



HAL
open science

Endocytosis-driven gold nanoparticle fractal rearrangement in cells and its influence on photothermal conversion

Vladimir Mulens-Arias, Alice Balfourier, Alba Nicolás-Boluda, Florent Carn, Florence Gazeau

► To cite this version:

Vladimir Mulens-Arias, Alice Balfourier, Alba Nicolás-Boluda, Florent Carn, Florence Gazeau. Endocytosis-driven gold nanoparticle fractal rearrangement in cells and its influence on photothermal conversion. *Nanoscale*, 2020, 12 (42), pp.21832-21849. 10.1039/D0NR05886F . hal-03092795

HAL Id: hal-03092795

<https://hal.science/hal-03092795>

Submitted on 2 Jan 2021

HAL is a multi-disciplinary open access archive for the deposit and dissemination of scientific research documents, whether they are published or not. The documents may come from teaching and research institutions in France or abroad, or from public or private research centers.

L'archive ouverte pluridisciplinaire **HAL**, est destinée au dépôt et à la diffusion de documents scientifiques de niveau recherche, publiés ou non, émanant des établissements d'enseignement et de recherche français ou étrangers, des laboratoires publics ou privés.



Cite this: DOI: 10.1039/d0nr05886f

Endocytosis-driven gold nanoparticle fractal rearrangement in cells and its influence on photothermal conversion†

Vladimir Mulens-Arias,^{a,b} Alice Balfourier,^a Alba Nicolás-Boluda,^a Florent Carn^a and Florence Gazeau¹  [✉]

Cellular endocytosis and intracellular trafficking of nanoparticles induce dynamic rearrangements that profoundly modify the physical properties of nanoparticle and govern their biological outcomes when activated by external fields. The precise structure, organization, distribution, and density of gold nanoparticles (AuNPs) confined within intracellular compartments such as lysosomes have not been studied comprehensively, hampering the derivation of predictive models of their therapeutic activity within the cells of interest. By using transmission electron microscopy and small-angle X-ray scattering, we have determined that canonical spherical citrate-coated AuNPs in the 3–30 nm size range form fractal clusters in endolysosomes of macrophages, endothelial cells, and colon cancer cells. Statistical analysis revealed that the cluster size and endolysosome size are correlated but do not depend on the size of AuNPs unless larger preformed aggregates of AuNPs are internalized. Smaller AuNPs are confined in greater numbers in loose aggregates covering a higher fraction of the endolysosomes compared to the largest AuNPs. The fractal dimensions of intracellular clusters increased with the particle size, regardless of the cell type. We thus analyzed how these intracellular structure parameters of AuNPs affect their optical absorption and photothermal properties. We observed that a 2nd plasmon resonance band was shifted to the near-infrared region when the nanoparticle size and fractal dimensions of the intracellular cluster increased. This phenomenon of intracellular plasmon coupling is not directly correlated to the size of the intralysosomal cluster or the number of AuNPs per cluster but rather to the compacity of the cluster and the size of the individual AuNPs. The intracellular plasmon-coupling phenomenon translates to an efficient heating efficiency with the excitation of the three cell types at 808 nm, transforming the NIR-transparent canonical AuNPs with sizes below 30 nm into NIR-absorbing clusters in the tumor microenvironment. Harnessing the spontaneous clustering of spherical AuNPs by cells might be a more valuable strategy for theranostic purposes than deploying complex engineering to derive NIR-absorbent nanostructures out of their environment. Our paper sheds light on AuNP intracellular reorganization and proposes a general method to link their intracellular fates to their *in situ* physical properties exploited in medical applications.

Received 10th August 2020,
Accepted 6th October 2020

DOI: 10.1039/d0nr05886f

rsc.li/nanoscale

Introduction

It is documented that the biological environment can change the chemical and physical properties of nanoparticles leading to the modification of their biological behavior and theranos-

tic efficiency. This effect is mainly due to the protein corona,^{1–4} and changes in electrolyte concentration⁵ and pH within the targeted fluids and tissues;⁶ for example, the tumor microenvironment,⁷ and the intracellular endosome/lysosome compartments, hereafter referred to as endolysosome, when the particles are internalized by cells. The context-dependent nanoparticle properties have been well established for iron oxide magnetic nanoparticles, *i.e.*, the intracellular aggregation of nanoparticles result in magnetic dipole interactions and impairment of rotational motion that dramatically affect the magnetic dynamics of iron oxide nanoparticles and lower their heating efficiency under an alternating magnetic field.^{8–10} However, less attention has been paid to the intracellular fate

^aLaboratoire Matière et Systèmes Complexes, UMR 7075, CNRS and Université de Paris, 10 Rue Alice Domon et Léonie Duquet, 75205 Paris Cedex 13, France.

E-mail: florence.gazeau@univ-paris-diderot.fr

^bDepartment of Immunology and Oncology, National Center for Biotechnology/CSIC, Darwin 3, Cantoblanco Campus, 28049 Madrid, Spain

†Electronic supplementary information (ESI) available. See DOI: 10.1039/d0nr05886f



of gold nanoparticles (AuNPs), even though their intracellular trafficking can also change their structural and optical features and thus, AuNPs interact with excitation fields and affect the surrounding biological structures. The efficacy of AuNPs as imaging tracers, photothermal agents, radiosensitizers, and photosensitive agents will strongly depend on their intracellular distribution and rearrangement within the cells. Within the biological environment, such as intracellular compartments, AuNPs can transit through different degrees of aggregation.¹¹ When 100 nm AuNPs transit through intracellular compartments, their spectral profile varies in a concentration- and time-dependent manner in human breast carcinoma Sk-Br-3 cells, recordable by hyperspectral microscopy, suggesting a transient change in plasmon behavior.¹¹ This phenomenon seems to be related to the AuNP aggregation as found by Curry *et al.* using anti-EGFR-capped AuNPs for the intracellular imaging of EGFR: anti-EGFR antibody-capped AuNPs aggregated on cell membranes, while control antibody-capped AuNPs appeared as single-dispersed.¹² Furthermore, AuNPs with different sizes might be internalized differently depending on the cell types of the tumor microenvironment, thereby conditioning their photothermal and photoacoustic efficiency,^{13,14} as well as photodynamic therapy and radiosensitization effects.¹⁵

Gold nanoparticles are among the most exploited nano-sized materials in biomedical approaches for cancer theranosis,^{16–18} mostly due to the wide possibilities for chemical modification and tunable optical and thermal capacities.^{19–23} The typically localized surface plasmon resonance (LSPR) peak in the transverse mode (~525 nm) of spherical AuNPs limits their use in light-induced thermal ablation because the wavelengths needed to efficiently engage plasmon resonance fall within the visible spectrum; they show short tissue penetration capacity owing to the light scattering of the surrounding tissues and the absorption by natural chromophores. However, in an attempt to induce a red-shift toward the first biological near-infrared (NIR) window, spherical AuNPs have been engineered to facilitate the plasmon coupling of nanoparticles.^{24,25} The plasmon coupling occurs when AuNPs get close enough so that the collective resonance of individual electron clouds can happen, leading to a redshift of the LSPR band in transverse mode or the appearance of a secondary LSPR band in the longitudinal mode within the NIR range.^{26–28} This phenomenon is characteristic of noble metal nanostructures, including gold nanoparticles,²⁸ and is the basis for plasmonic sensors^{29,30} and thermal ablation approaches.^{31,32} Thus, a NIR light source penetrating deeper in tissues than visible light can be used to trigger photothermal conversion, inducing more efficient and selective heating. Aggregation-induced plasmon coupling can be efficient enough to generate photoacoustic signals, even for small sizes of AuNP (<30 nm) with the advantages of better penetrating the tumor and facilitating elimination or degradation, as compared to larger NIR-absorbing gold nanorods or nanostars.^{33–35} Since AuNP endocytosis can lead to highly dense clustering within intracellular compartments,^{36,37} it

might narrow interparticle gaps (<2 nm)²⁶ and facilitate the plasmon coupling phenomenon only *in situ* inside the cells. The plasmon coupling effect and its association with the appearance of a secondary LSPR were well demonstrated by the conformation of discrete AuNP-based structures, *i.e.*, dimers and trimers,³⁸ or more complex self-assemblies of gold nanoparticles into linear, globular, or fractal clusters.^{39,40} However little is known about the rearrangement that intracellular confinement might impose on AuNP of different sizes, and, more importantly, how this process influences AuNP light-to-heat conversion and photothermia in the cellular environment.

The purpose of our study was thus to correlate the structural properties of intracellular AuNP clusters in endolysosomes with their optical and photothermal properties. To shed light on these effects of cell internalization, we propose a comprehensive investigation of the intracellular distribution and endocytosis-induced aggregation of canonical citrate-coated spherical AuNPs with diameters ranging from 3 to 30 nm in three different cell types that are present in the tumor microenvironment, *i.e.*, macrophages, endothelial cells, and colon cancer cells. We characterize in detail the structure and density of AuNP rearrangements triggered by endosomal uptake and lysosomal confinement, and question how these rearrangements depend on nanoparticle size and cell type. We thus address the question of how intracellular AuNP confinement influences their optical properties and photothermal conversion efficiency in terms of photothermal therapy (PTT) and photoacoustic imaging (PAI) applications.

Experimental section

Cell culture

Murine cell line macrophage-like cells RAW264.7 (ATCC, TIB-71), and SV40-transformed endothelial cells SVEC4-10 7 (ATCC, CRL-2181), as well as primary murine colorectal carcinoma cells, CT26 (ATCC, CRL-263) were cultured in DMEM supplemented with 10% fetal bovine serum (FBS), penicillin/streptomycin, L-glucose and sodium pyruvate.

Citrate-coated gold nanoparticle synthesis

Gold nanoparticles (AuNPs) were synthesized following a Turkevich protocol as stated elsewhere,⁴¹ based on the synthesis of 10 nm gold seeds followed by sequential seed growth. Briefly, sodium citrate (97 mg) was dissolved in 150 mL of MilliQ water and boiled under magnetic stirring for 15 minutes, followed by the addition of 1 mL of pre-heated 25 mM gold chloride solution. After 10 minutes, the reaction was cooled to 70 °C and then diluted by extracting 55 mL of the AuNP solution and replenishing with MilliQ water (53 mL) and sodium citrate (2 mL, 60 mM). Gold chloride (1 mL, 25 mM) was added, followed by a second addition after 30 min. The procedure was repeated until the desired AuNP sizes were obtained, *e.g.*, once for the 16 nm, 3 times for the 30 nm, 7 times for the 40 nm. The smallest AuNPs (3 and



11 nm) were synthesized in the presence of tannic acid.⁴² Briefly, sodium citrate (97 mg) and potassium carbonate (20.7 mg) were dissolved in 150 mL of water and mixed with a tannic acid solution (1 mL, 2.5 mM). After heating at 70 °C under magnetic stirring, 1 mL of 25 mM gold chloride solution was added, and the reaction was stopped when the solution turned orange.

$$\text{Viability}(\%) = \frac{[\text{AuNP-treated cell fluorescence}] - [\text{medium fluorescence}]}{[\text{untreated cell fluorescence}] - [\text{medium fluorescence}]} \times 100.$$

AuNPs were characterized by transmission electron microscopy (TEM). TEM images of aqueous dispersions were obtained with a JEOL JEM-1400PLUS transmission electron microscope operating at an acceleration of 120 kV (Institut Jacques Monod, Paris, France).

Synthesis of 5FU-AuNP complex

Citrate-coated AuNPs were diluted in ddH₂O (40 μg ml⁻¹) and mixed with an equal volume of aqueous solution of 5-fluorouracil chemotherapeutic drug (5-FU) (10 mg ml⁻¹) for a final [Au]:[5-FU] ratio of 20 μg ml⁻¹:5 mg ml⁻¹. The mixture was incubated for up to 24 hours at room temperature under constant shaking. The formation of the complex was monitored by SAXS, UV-visible absorbance, and cryo-TEM imaging.

Cell TEM imaging

After incubation with AuNPs for 24 hours, cells were harvested, washed 3 times with PBS 1×, and resuspended in fixation buffer (0.1 M sodium cacodylate, 2.5% glutaraldehyde). Cell suspensions were mixed gently for 1 hour at 4 °C. After they were washed twice, the cells were resuspended in 0.1 M sodium cacodylate buffer until the TEM procedure. Samples were then contrasted with Oolong Tea Extract (OTE) 0.5% in cacodylate buffer, post-fixed with 1% osmium tetroxide containing 1.5% potassium cyanoferrate, gradually dehydrated in ethanol (30% to 100%) and gradually substituted in a mix of ethanol-Epon and embedded in Epon (Delta microscopie – Labège, France). Thin sections (70 nm) were collected on 200 mesh copper grids and counterstained with lead citrate. Grids were examined with a Hitachi HT7700 electron microscope operated at 80 kV (Elexience – France), and images were acquired with a charge-coupled device camera (AMT) (Université Paris-Saclay, INRAE, AgroParisTech, GABI, 78350, Jouy-en-Josas, France). To determine the two-dimensional (2-D) fractal dimensions, cryo-TEM images were processed using ImageJ software (NIH, USA). Nanoparticle clusters were isolated (cropped), converted into 8-bit, thresholded, and then converted into binary and analyzed by the Fractal Box Counting tool, with box sizes of 2, 3, 4, 6, 8, 16, 32, and 64.

Particle uptake and cytotoxicity assay

Subconfluent cells were incubated for 24 hours with an increasing concentration of AuNPs in complete DMEM. For the last 4 h, Presto Blue Cell Viability reagent was added (1/10 final dilution; Presto Blue Cell Viability Reagent, A13261; Invitrogen). Fluorescence was measured with a 535 nm exci-

tation filter and a 615 nm emission filter. The fluorescence of complete DMEM incubated with Presto Blue was used as the background control. Cell viability was calculated according to the following formula:

Localized surface plasmon resonance (LSPR) band analysis

Cells were cultured with 10 μg ml⁻¹ AuNP for 24 h, harvested, and thoroughly washed with cold PBS 1×. Cells were then resuspended in 100 ml PBS 1×, and the absorbance was profiled in the range 350 nm–800 nm with a Multimode Plate Reader (EnSpire, Perkin-Elmer). Triplicate samples were analyzed and PBS 1× was used as the blank. To isolate LSPR bands and get rid of the absorption spectra of the cells (without AuNPs) primary data were normalized as follows:

(1) Blank absorbance was subtracted:

$$\text{Absorbance}_{\text{subs}} = \text{Absorbance}_{\text{sample}} - \text{Absorbance}_{\text{PBS}}$$

(2) Normalization against the absorbance value at 449 nm of the cell absorption spectrum (without AuNPs)

$$\text{Absorbance}_{\text{multiplication}} = \text{Absorbance}_{\text{subs}} \times \text{Absorbance}_{\text{subs}}(449 \text{ nm})$$

(3) Normalization by subtracting this value from the sample absorbance:

$$\text{Absorbance}_{\text{normalized}} = \text{Absorbance}_{\text{subs}} - \text{Absorbance}_{\text{multiplication}}$$

In vitro photothermia in cells loaded with AuNPs

Cells were incubated with 10 μg ml⁻¹ AuNP for 24 hours in 6-well cell culture plates. Cells were then harvested accordingly, washed with PBS 1×, and resuspended in 100 μl of PBS 1× (500 μl tube). The absorbance was measured in a multimode plate reader (PerkinElmer, EnSpire), and cells were immediately subjected to either a 680 nm or 808 nm beam laser for 5 min (fluence of 1 or 3.57 W cm⁻², height 4 cm from the liquid/air interface, Laser Diode Drivers, BWT). The temperature was recorded with an infrared camera SC7000 from FLIR Systems.

Small-angle X-ray scattering (SAXS) characterization

For SAXS analysis, AuNPs, AuNP-5FU complexes, or cells loaded with 10 μg ml⁻¹ AuNP or AuNP-5FU for 24 h were placed in sealed quartz capillaries on the SWING synchrotron beamlines (SOLEIL synchrotron at Saint-Aubin, France) with a



configuration of $D = 2.1$ m and $\lambda = 1 \text{ \AA}$ to get a q -range from 4.8×10^{-3} to 0.52 \AA^{-1} . SAXS files were analyzed after subtraction with the SasView Software (NSF DANSE), by fitting, when stated, according to the shape-independent mass fractal model. This model relies on the scattering from fractal-like aggregates of sphere-shaped building blocks, here AuNPs, of radius R_0 according to the following equation:⁴³

$$I(q) = \phi \times V_{\text{block}} \times (\rho_{\text{block}} - \rho_{\text{solvent}})^2 \times P(q)S(q) + \text{background}(1)$$

where ϕ refers to the volume fraction of the spherical building block, $V_{\text{block}} = \frac{4}{3} \times \pi R_0^3$ is the volume of a single building block, ρ_{block} is the scattering length density of AuNPs (Au, $6.4608 \times 10^{-6} \text{ \AA}^{-2}$), and ρ_{solvent} is the scattering length density of solvent that we considered close to water (H_2O , $9.4691 \times 10^{-6} \text{ \AA}^{-2}$). The form factor $P(q)$ and the structure factor $S(q)$ are calculated as follows:

$$P(q) = F(qR_0)^2$$

$$F(x) = \frac{3[\sin(x) - x \cos(x)]}{x^3}$$

$$S(q) = 1 + \frac{D_f \Gamma(D_f - 1)}{[1 + 1/(q\zeta)^2]^{\frac{D_f-1}{2}}} \times \frac{\sin[(D_f - 1) \tan^{-1}(q\zeta)]}{(qR_0)^{D_f}}$$

where ζ is the correlation length representing the size of the aggregate and D_f is its fractal dimension.

Photoacoustic imaging (PAI) of AuNP-loaded cells

To evaluate the PAI contrast efficiency of AuNP-loaded cells, cells incubated with $10 \mu\text{g ml}^{-1}$ AuNPs for 24 hours were harvested, washed, and resuspended in $50 \mu\text{l}$ PBS $1\times$ and embedded in $50 \mu\text{l}$ of 1% agarose to prepare phantoms. Phantoms were then scanned with a photo-acoustic imaging system (VeVo® LZR SW2.2.0, VisualSonics, Inc., FUJIFILM, Institut Jacques Monod, Université Sorbonne Paris Cité, Paris, France) using a linear array transducer LZ550 (36 MHz center frequency, 32–55 MHz bandwidth, $44 \mu\text{m}$ axial resolution, $14 \times 15 \text{ mm}^2$ image size) to obtain PA images. Images were analyzed using VeVo@Lab and ImageJ software.

In vivo colon carcinoma CT26 tumor model for photothermal analysis

Animal studies were conducted in agreement with the French guidelines for animal care in compliance with procedures approved by the ethical committee from Université Paris Diderot for animal research. CT26 tumor-bearing BALB/c mice (6–8 weeks old), established by subcutaneous injection of 1.5×10^6 CT26 cells (tumor size $\geq 5 \text{ mm}$), were randomized into two groups that experienced (i) only 808 nm laser irradiation at $\sim 2 \text{ W cm}^{-2}$ for 15 min (height from tumor skin 4 cm, Laser Diode Drivers, BWT) ($n = 5$), and (ii) $40 \mu\text{g}$ per mouse AuNP_{16 nm} intratumor injection, followed 24 h later by 808 nm laser irradiation at $\sim 2 \text{ W cm}^{-2}$ for 15 min ($n = 5$). The skin surface temperature was recorded with an infrared camera SC7000 from FLIR Systems during the treatment.

Statistical analysis

Data are presented as mean \pm SEM, and the number of samples and independent experiments are stated in each figure caption for precision. When stated, all groups were compared to the control by the one-way ANOVA test with the Bonferroni *post hoc* test; $*p < 0.05$, $**p < 0.01$, and, $***p < 0.001$, 95% confidence.

Principal component analysis and Pearson correlation coefficients have been calculated with R 3.6.0, with the PCA function of the FactoMineR package with default parameters, and the cor function of the library stats. The heatmap was generated with the pheatmap function of the pheatmap package.

Results and discussion

Cell internalization of spherical gold nanoparticle induces endolysosome-limited fractal aggregation depending on AuNP size and cell type

We first studied the internalization and intracellular arrangement of citrate-coated AuNPs of 3 to 30 nm in diameter (Fig. S1†) in different cell types reflecting the complexity of the tumor microenvironment, *i.e.* macrophages (RAW264.7), endothelial cells (SVEC), and colon carcinoma tumor cells (CT26). Macrophages are well known for their ability to take up nanomaterials and survey peripheral tissues (including tumors) for threats;^{44,45} these cells, therefore, are the first encounter for the nanomaterials and key actors of the tumor immune response. It has been reported that macrophages can change their phenotype and functionalities (*i.e.* adhesion, migratory or invasion ability) upon internalization of AuNPs in a size-dependent manner.⁴⁶ AuNP internalization in the murine RAW264.7 macrophage cell line did not induce a significant change in the cell metabolic activity after incubation with AuNP concentration up to $40 \mu\text{g mL}^{-1}$ for 24 hours (Fig. S2A†). Whatever the size of AuNPs ($10 \mu\text{g mL}^{-1}$, 24 hours incubation), we observed intracellular clustering of AuNPs within endolysosome compartments (Fig. 1A). To characterize the intracellular fate of the nanoparticles, we measured the size of the nanoparticles-containing endolysosomes and the size, the density, and the structure of AuNP clusters within each endolysosome by analysis of TEM pictures. Only endolysosomes with clearly visible membrane structures were analyzed. AuNP internalization induced changes in the endolysosome area, as determined by TEM imaging, depending on the AuNP core size (Fig. 1B). Unlabelled cells display endolysosomes with an average area of $\sim 0.5 \mu\text{m}^2$. However, 11 nm-AuNP and 16 nm-AuNP-containing endolysosomes displayed a greater average area (1.5 and $1.2 \mu\text{m}^2$, respectively) than the 3 nm-AuNP and 30 nm-AuNP-containing endolysosomes (0.5 and $0.8 \mu\text{m}^2$, respectively), but these variations are not statistically significant. In contrast, the average cluster diameter increased significantly for the AuNPs with sizes above 16 nm as shown in Fig. 1C (239 nm and 250 nm cluster size for 16 and 30 nm-AuNPs *versus* 169 nm and 150 nm cluster size for 3 and 11 nm-AuNPs). A detailed analysis of the number of nanoparticles per



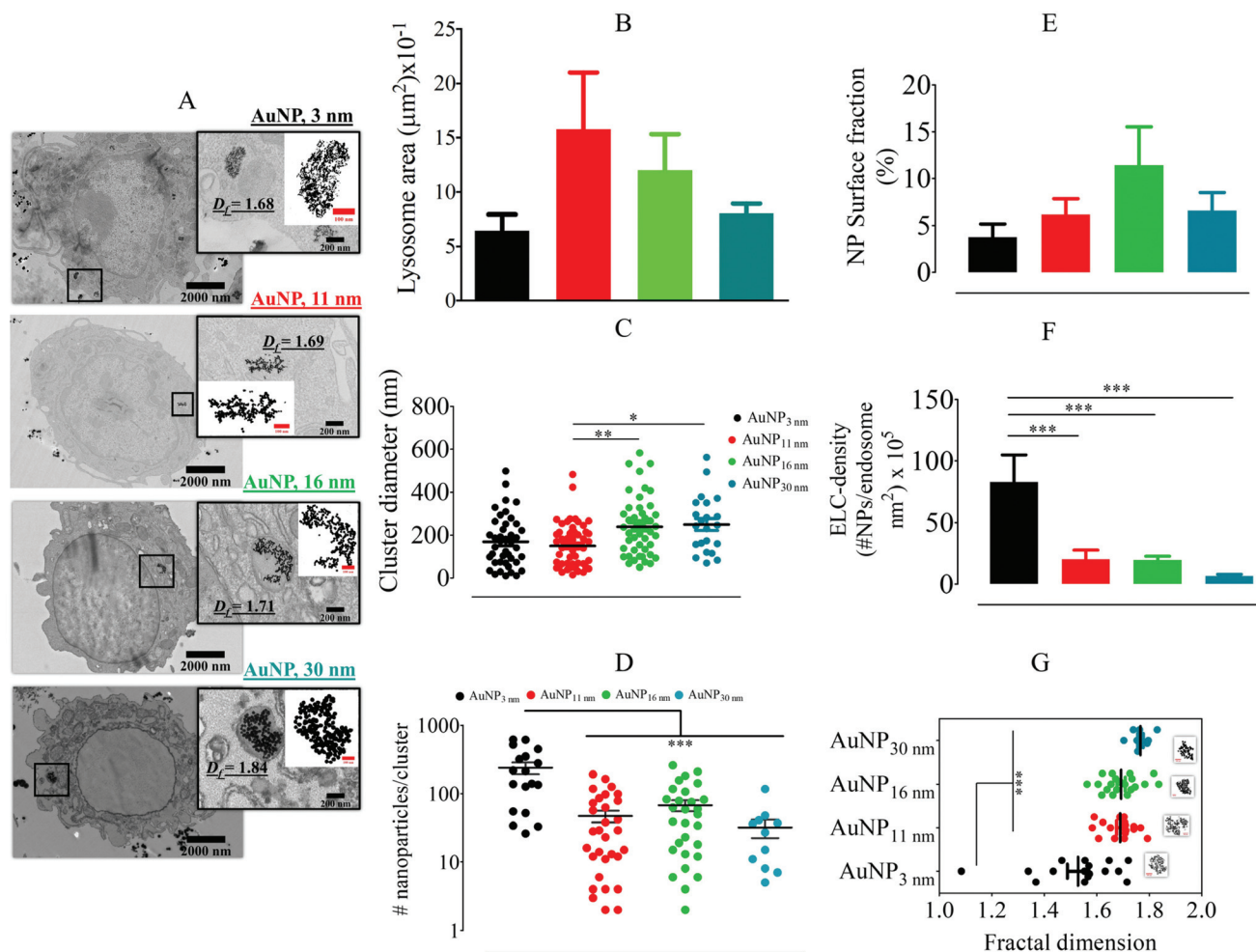


Fig. 1 The internalization of gold nanoparticles by the murine macrophage-like cell line. (A) TEM imaging of AuNP-loaded RAW264.7 cells; the insets emphasize intracellular AuNP clusters and the corresponding binary transformation for fractal arrangement analysis, where D_f stands for the fractal dimension. (B) Area of NPs-containing endolysosomes. (C) Intracellular cluster diameter. (D) The number of nanoparticles per intracellular cluster. (E) Surface fraction covered by intracellular AuNP as determined by TEM imaging. (F) Endolysosome-limited cluster density (ELC density) of AuNP. (G) 2-D fractal dimensions of intracellular AuNP clusters; insets represent exemplary binary fractals. Significance, * $p < 0.05$, ** $p < 0.01$, *** $p < 0.001$; one-way ANOVA test, with Bonferroni post-test for the comparison of all pairs of columns.

intracellular cluster revealed a clear dependence on nanoparticle size. The mean nanoparticle number per cluster decreased from 197 for 3 nm-AuNPs to 32 for 30 nm-AuNPs (Fig. 1D). Another important aspect refers to the endolysosome surface fraction (2D) covered by nanoparticle clusters, as it reflects the extent of confinement in 3D. The 16 nm diameter appeared to be an optimal size for covering >10% of the 2D lysosomal surface, while the other nanoparticle size covered <10% (Fig. 1E); as a result, the endolysosome-limited cluster density (number of AuNP/endolysosome area), decreased for larger AuNPs (Fig. 1F). Interestingly, both nanoparticle numbers per cluster and cluster diameter exhibited high variability within one condition suggesting a dynamic AuNP intracellular transit, whereby different AuNP clusters are in different intracellular transit steps. Intracellular localization (endosome maturation status, fusion with lysosomes), time of exposition, and the difference in endosomal compartment pH

and protein content might account for this variability, hence displaying a step-wise and multiple pathway internalization. Liu M *et al.* reported an early stage of AuNP internalization where most of the nanoparticles appeared as single particles, and as endosomes migrated and matured, AuNP clusters started forming.³⁶ We did not observe single particles, which can be related to the late observation of the cells by TEM (24-hour time-point).

The structural arrangement of particles was characterized by measuring the fractal dimensions of AuNP aggregates. Two complementary methodologies were implemented for this purpose: the first one relies on the previously described TEM micrographs using the Bow count method on ImageJ,⁴⁷ which provides a 2D fractal dimension for each intralysosomal cluster (Fig. 1G and insets inside). The second is based on small-angle X-ray scattering (SAXS), which gives access to the 3D fractal dimension of nanoparticle aggregates, averaged over



the whole cell population. The SAXS intensity signal of non-loaded cells was first subtracted from the intensity signal of AuNP-loaded cells (Fig. S3,† left) and then fitted with the shape-independent mass fractal model,^{48,49} considering that the building blocks of the clusters are monodispersed spheres with the same average size as AuNPs. Under these conditions, the slope of the SAXS signal at the lower q -values (Fig. S3,† right) gives an estimation of the 3D fractal dimension of the AuNP cluster in the whole cell population. Contrastingly, the AuNPs incubated in culture medium without cells displayed a flat intensity signal at low q -values, indicating the dispersed state of the colloidal suspension. Therefore, the fractal arrangement in cells is related to cell processing by endocytosis of nanoparticles rather than to a serum protein-induced AuNP agglomeration before nanoparticle internalization. The SAXS measurements in cells therefore provide a clear indication of the intracellular fractal structure of the AuNP agglomerates, confirming the TEM observations. Note that due to the lack of signal for the smallest particles, the SAXS measurements were exploitable only for the 16 nm and 30 nm sizes. Quantitatively, TEM imaging provided 2D fractal dimensions that increased with AuNP particle size in macrophages (AuNP diameter of 3, 11, 16, and 30 nm rendered 2D fractal dimensions of 1.52, 1.68, 1.68, and 1.75, respectively). Nonetheless, the 3D fractal dimension deduced from SAXS appeared to be higher, with a value of 2.97 and 2.90 for the 16 and 30 nm AuNPs, respectively. Note that the analysis of the power law domain in SAXS profile is limited to a narrow q range, which makes a valuable determination of 3D fractal dimension difficult. Overall, this detailed analysis of AuNP-containing endolysosomes shows the increasingly compact structure of nanoparticle clusters in endolysosomes when particle size increases, associated with an increased cluster diameter. Despite the less compact structure, the 3 nm-sized AuNPs maximize the number of particles per cluster and per endolysosome. The 16 nm AuNPs occupied the maximum surface fraction.

To ascertain whether the endosomal confinement-driven AuNP fractal aggregations depend on the targeted cell type, a similar TEM analysis was performed on the murine endothelial cell line SVEC4-10 (Fig. S4A†), which is an important barrier for the extravasation of nanoparticles. Again, AuNPs internalization did not induce significant cell death as determined by the metabolic rate (Fig. S2B†). The area of endothelial cell nanoparticles-containing endolysosomes was comparable to that of macrophages, with no significant influence of particle size (Fig. S4B†). However, AuNP clusters in SVEC4-10 cells appeared to be smaller than in macrophages, with an average diameter ranging from 106 to 215 nm only. In contrast to macrophages, the largest clusters were found for the 3 nm-AuNPs (Fig. S4C†). The number of AuNPs per intracellular cluster decreased with increasing nanoparticle size, similar to macrophages, but with a lower number of AuNPs per cluster (average number from 14 to 176 AuNPs as compared to 32 to 240 for macrophages) (Fig. S4D†). The endolysosome surface fraction (2D) of nanoparticle cluster was also lower than in

macrophages, covering at most 3% of the endolysosome surface for the 16 nm-AuNPs. However, the size tendencies observed for the endolysosome limited cluster density (Fig. S4F†) and the 2D fractal dimension (Fig. S4G†) are consistent between endothelial cells and macrophages. The intracellular aggregate features are comparable between macrophages and endothelial cells, except for the density, which remains higher in macrophages.

The comparison of the processing of AuNPs between endothelial cells and macrophages underscores the particularity of 3 nm-AuNPs. For macrophages, the 3 nm-AuNPs are enclosed in the smallest endolysosome size with also the smallest cluster diameter, whereas for endothelial cells, they present the highest endolysosome and cluster sizes. This difference can be linked to the endocytosis pathways (phagocytosis, pinocytosis, and receptor-mediated endocytosis) that could have different influences between cell types.⁵⁰ Moreover, macrophages are known to have a higher endocytosis rate than other cell types,^{44,45} which could explain why their endolysosomes contain larger AuNP clusters covering a higher surface fraction of the endolysosome.

The same analyses were performed on the murine colorectal carcinoma cell line CT26, as a model of cancer cell behavior. The experiment was limited to the 16- and 30 nm-AuNPs sizes but was extended to pre-aggregated 16 nm and 30 nm-AuNPs structures obtained by combination with the anticancer drug 5-fluorouracil (5-FU). These drug-NP clusters were used here to investigate whether a pre-aggregated state of AuNPs can change their fate and intracellular structure once inside the cells. AuNP-5FU complexes were synthesized by mixing 16- and 30 nm-AuNP with the 5-FU for 24 hours. The SAXS profile analysis showed the fractal structure of the as-formed AuNP-5FU complexes with mass 3D fractal dimensions of 1.85 and 2.06, respectively, with the 16 nm- and 30 nm AuNPs building blocks (Fig. S5A and B†). AuNP-5FU complexes were then incubated with cells at the same concentration as the single AuNPs.

As shown in Fig. 2A, the colon cancer cells exhibited pre-aggregated AuNP-5FU complexes and AuNPs-loaded endolysosomes, but noticeable differences were observed. Endolysosomes were 1- to 4-fold larger when loaded with AuNP-5FU complexes rather than AuNPs (Fig. 2B). The intracellular cluster size (Fig. 2C) and the number of AuNPs per cluster (Fig. 2D) also considerably increased with pre-aggregated AuNP-5FU complexes. Consequently, the endolysosome surface fraction (2D) covered by nanoparticle clusters were augmented from 2.5% for 16 nm AuNPs to 8.5% for the 16 nm AuNP-5FU complex (Fig. 2E), and the ELC-density also increased for the AuNP-5FU complexes (Fig. 2F). The average fractal dimension of the aggregates in cells also tended to be higher when nanoparticles were pre-aggregated (Fig. 2G). This observation was confirmed by SAXS measurements in 16 nm-AuNP and 16 nm-AuNP-5FU-loaded CT26 cells: the former resulted in a 3D fractal dimension of 2.33, *versus* 2.44 for the AuNP-5FU complexes (Fig. S6†). Overall, it is clear that the pre-aggregation of AuNPs by complexation with the 5-FU drug



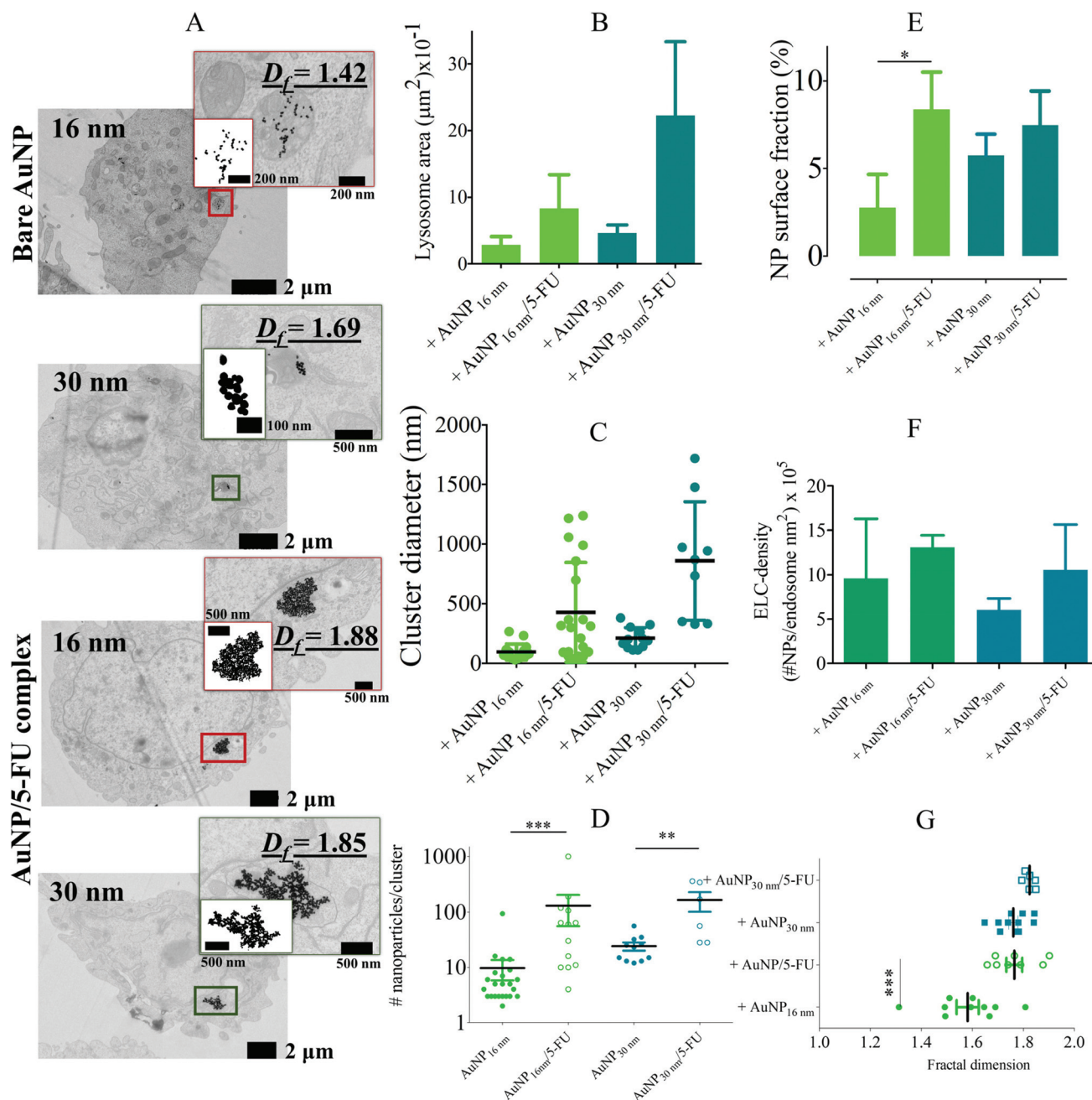


Fig. 2 Internalization of 5FU-pre-aggregated or dispersed gold nanoparticles by the murine colorectal cell line, CT26. (A) TEM imaging of AuNP-loaded CT26 cells; the insets emphasize intracellular AuNP clusters and the corresponding binary transformation for fractal arrangement analysis. (B) The area of NPs-containing endolysosomes as determined by TEM imaging. (C) Intracellular cluster diameter. (D) The number of nanoparticles per intracellular cluster. (E) Surface fraction covered by intracellular AuNP. (F) Endolysosome-limited cluster density (ELC density) of AuNP. (G) 2-D fractal dimensions of intracellular AuNP clusters. Significance, * $p < 0.05$, ** $p < 0.01$, *** $p < 0.001$; one-way ANOVA test, with Bonferroni post-test for comparison of all pairs of columns.

before cell internalization tends to optimize the lysosomal density of AuNPs while also changing the endolysosome size.

Considering the single AuNP condition in CT26 cells, the results are consistent with other cell type characterization, indicating relative homogeneity between cell types. However, we noticed that in this study, contrary to previous observations on macrophages and endothelial cells with isolated AuNPs

from 3 to 30 nm, the endolysosome size adapted to its contents in pre-aggregated AuNP-loaded CT26 cells. The intracellular AuNP-5FU clusters exceeded the size of the clusters achieved by the isolated AuNPs and the endolysosome size also increased. Hence, endolysosome shape adjustment might not be cell-type dependent but probably appears above a certain size of intracellular cluster diameter, which could be



roughly estimated to 500 nm. This suggests that lysosomal shape adjustment, which occurred only above a certain size of the internalized structure and not for isolated NPs of 3 to 30 nm, could be a general process independent of nanoparticle characteristics.

Overall, our comprehensive investigation sheds light on the endocytosis-driven fractal aggregation endured by the different sizes of AuNPs and the preformed AuNP aggregates, which occurs independently of the cell type. The intralysosomal nanoparticle fractal dimension increases with the size of AuNPs and the preformed aggregates. The number of particles per cluster diminishes when increasing particle size. However, the surface fraction occupied by AuNPs in endolysosomes, an important parameter for the local effect of AuNP activation, is maximized in the different cell lines for the single or pre-aggregated 16 nm-AuNPs.

The detailed study of AuNP intracellular distribution is of particular importance to modeling and predicting the physical and subsequent biological effects of radiosensitization by high atomic number nanoparticles^{15,51,52} that depend on their local arrangement, the density of the high Z materials to focus the X-ray beam and its proximity to vital cellular structures. It can be a valuable basis for the future modeling of radiosensitization effects. However, in the present study, we focus our investigation on another aspect that also dramatically depends on the intracellular local organization of nanoparticles: the photothermal activity of AuNPs.

Intracellular fractal organization of AuNPs induces plasmon coupling, the appearance of a secondary LSPR absorption mode, and enhanced photothermal properties

The occurrence of plasmon coupling is based on the hybridization of the resonance of individual particles leading to a peak wavelength shift toward the red. Having characterized in detail the endocytosis-driven cluster formation, we thus analyzed the implications for intracellular plasmonic AuNP properties. The extinction spectra of AuNP (3–30 nm)-loaded macrophages, endothelial cells, and colon carcinoma cells were acquired by a UV-vis spectrometer and normalized using the absorption spectra of non-loaded cells as stated in the Materials and Methods section. This treatment emphasizes the contribution of the internalized AuNPs to the absorption spectrum, eliminating the biological material-derived extinction spectrum. It is worth noting that we observed a secondary LSPR for the 11, 16, and 30 nm-AuNPs in three cell types; however, the internalized 3 nm-AuNPs exhibited a single redshifted LSPR peak (Fig. 3). The primary LSPR peak is visible for all AuNP diameters corresponding to the transverse plasmon mode of the spherical AuNPs. The secondary LSPR correlated positively with the AuNP diameter, *i.e.*, secondary LSPR ~659 nm, 689 nm, and 776 nm for 11 nm, 16 nm, and 30 nm-AuNP, respectively, in macrophages (Fig. 3A). Similar tendencies were observed for endothelial cells/colorectal cancer cells, with a peak displacement to 602/590 nm for the 3 nm-AuNP, and a second plasmon peak appeared at 650/630 nm, 674/675 nm,

and 722/720 nm for 11 nm, 16 nm, and 30 nm-AuNP, respectively (Fig. 3B and C). These displacements are lower than those observed in macrophages. The appearance of the secondary LSPR can then be attributed to the closeness of the AuNPs within intracellular clusters leading to the resonance between adjacent nanoparticle electric fields. This plasmon coupling effect was analyzed before in a library of synthetic AuNP aggregates and by numerical simulation, while coupled AuNPs PEI complexes were previously proved to be effective *in vitro* and *in vivo* for photothermal therapy and photoacoustic imaging.^{53–55} Here, the secondary LSPR around 700 nm, together with the reminiscent primary LSPR of spherical AuNPs was easily observed in the extinction spectra of AuNP-5FU complexes in suspension (Fig. S5C and D[†]), confirming that intracellular endocytosis-driven aggregation can result in similar plasmon coupling effects in comparison to the synthetic aggregates. Interestingly, when the preformed 16 nm AuNP-5FU complexes were internalized in cancer cells, the second LSPR was only shifted from 680 nm (Fig. S5C[†]) to 715 nm (Fig. S7A[†]). Nonetheless, cell internalization of the isolated 16 nm-AuNP induced an LSPR at 675 nm (Fig. S7B[†]). Although the preformed clusters of AuNPs were arranged into larger aggregates and endolysosomes as compared to the single AuNP (Fig. 2), the optical properties of both intracellular aggregates were not so different (Fig. S7[†]), which questions the idea of synthesizing plasmonic aggregates for intracellular photothermal therapy.

We thus investigated whether and to what extent intracellular plasmon coupling can affect the light-to-heat conversion in cells, a milestone for the efficacy of photothermal therapy in the tumor microenvironment.⁵⁶ Immediately after the UV-vis spectrum acquisition, the cell suspensions were irradiated with either a 680 or 808 nm laser for 5 min at a fluence of 3.57 W cm⁻² and the temperature increase was recorded by an infrared camera. The temperature increment ΔT in the AuNP-loaded macrophages was 28.6 °C to 35.2 °C upon 680 nm-laser irradiation, and 13.5 °C to 25.7 °C for the 808 nm-laser, depending on the AuNP diameter (Fig. 4A and D). While ΔT increased steadily with the AuNP core size upon 808 nm irradiation, it presented a maximum for 11 nm- and 16 nm-AuNP upon irradiation with 680 nm light. These results are in line with the extinction spectra shown in Fig. 5A, as the maximal secondary LSPR for both AuNPs is close to 680 nm, while the 30 nm-AuNP exhibits a secondary LSPR closer to 808 nm. In cancer cells, the temperature increased with the size of the nanoparticles upon 680 nm irradiation (Fig. 4C), in line with the optical absorption (Fig. 3C). AuNP-loaded endothelial cells exhibited a photothermal conversion trend upon 808 nm laser irradiation similar to that of AuNP-loaded macrophages (Fig. 4E). Nonetheless, 3 nm-AuNPs-loaded endothelial cells irradiated at 680 nm showed a higher ΔT than the other sizes in contrast to the rest of the tested cells (Fig. 4B). This could be due to the larger 3 nm-AuNP intracellular cluster observed in SVEC in comparison to the other nanoparticle size (Fig. S4C & F[†]). Importantly, we observed similar plasmon coupling phenomena using a 3.5-fold lower laser fluence (1 W



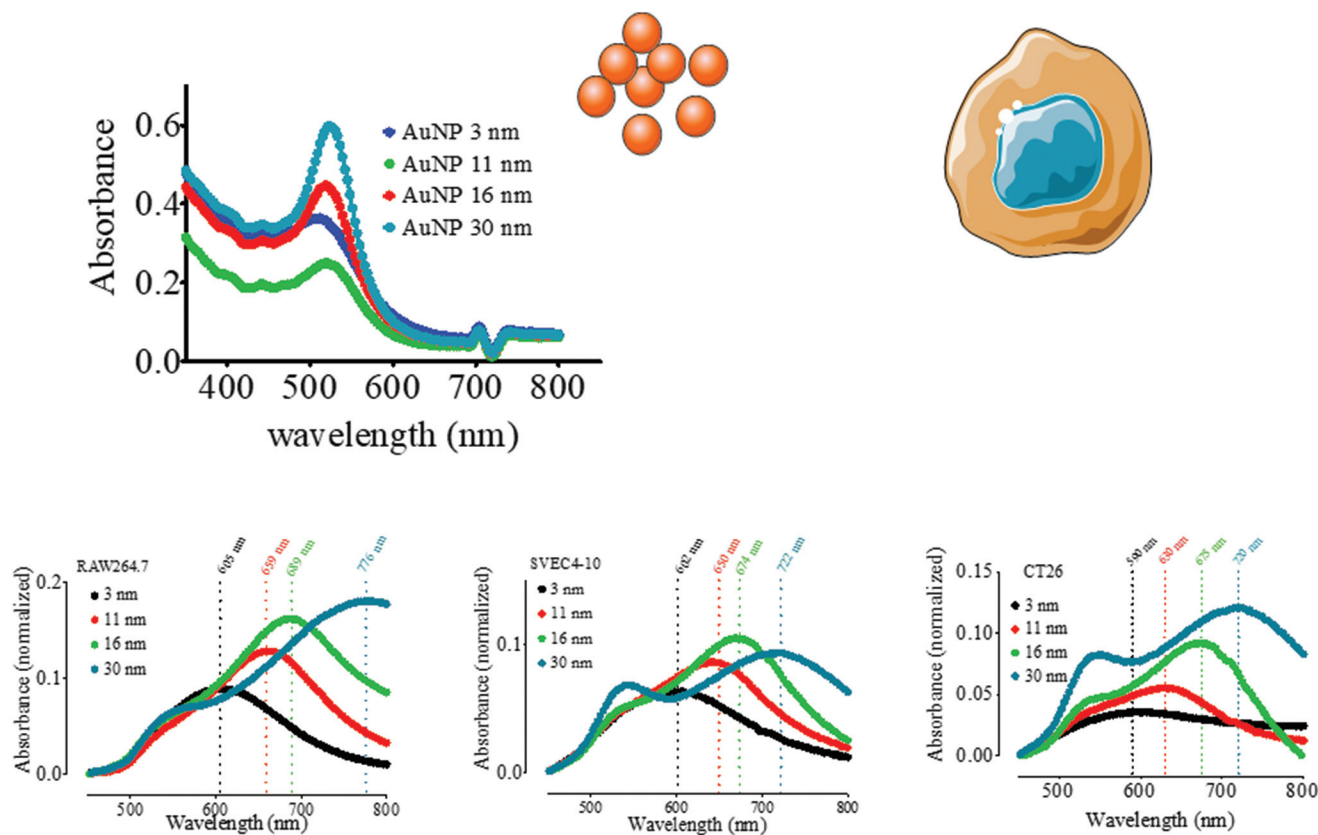


Fig. 3 UV-visible spectra of citrate AuNP before incubation with cells (A). UV-visible spectra of RAW264.7 macrophages (B), SVEC4.10 endothelial cells (C), and CT26 colon carcinoma cells (D) after the internalization of AuNPs of different sizes ($10 \mu\text{g ml}^{-1}$, 24 h) normalized by the absorption spectra of the respective cells without AuNPs. Highlighted wavelengths stand for the maximum secondary LSPR.

cm^{-2}) for RAW264.7 cells, suggesting that this effect occurs in a wide laser power range (Fig. S8†).

We also questioned the interest of using preformed AuNP aggregates showing plasmon coupling and enhanced absorption in the NIR range before internalization in cells. We thus compared the temperature increment in cancer cells loaded with 16 nm-AuNPs and with 16 nm AuNP-5FU complexes (Fig. S7B†) irradiated at 808 nm. The cell temperature was only slightly increased with the preformed clusters confirming the moderate advantage of pre-clustering before cell internalization for intracellular hyperthermia. It is worth noting that the preformed aggregates can heat outside the cells due to plasmon coupling under NIR light, whereas AuNPs that remain isolated before cell internalization will not heat. Thus, intracellular photothermal activation using isolated spherical NIR-transparent AuNPs can be seen as an ON/OFF process that requires both endolysosomal-limited clustering and light excitation to be effective.

This is particularly important for tumor therapy approaches using the photothermal activation of plasmonic nanostructures. Most studies and ongoing clinical trials focus on NIR-absorbent nanoparticles such as gold nanostars⁵⁷ or gold nanoshells⁵⁸ to induce highly efficient hyperthermia in the

tumor environment. However, only a few reports have addressed the impact that tumor cell internalization can have on the photo-thermal outcome in the complex environment of the tumors.^{57,59} Here, we have seen that intracellular clustering of NIR-transparent AuNPs could trigger efficient photothermal heating in three cellular components of the tumor microenvironment. It is worth noting that this complexity of gold nanoparticles and biological tissue interaction has been also addressed by developing an adaptive hyperspectral image algorithm. The training on the spectral behavior of gold nanoshells based on a spectral library allows the tuning of nanoparticle identification, whereupon it is possible to track gold nanoshells in *ex vivo* tissue samples.⁶⁰ Therefore, the changes in the plasmon within the biological milieu are not unique to NIR-invisible gold nanoparticles and can be used to identify nanoparticles within biological tissues. Considering that pre-aggregated AuNP can abolish tumor mass upon the conversion of NIR-light into heat,^{31,61,62} we then determined whether intratumor injection of NIR-transparent 16 nm-AuNP is sufficient to trigger photo-conversion of an 808 nm light in a head-to-head comparison with the preformed 16 nm-AuNP-5FU complexes (Fig. 5A). CT26 colorectal tumors were induced subcutaneously in immunocompetent mice and



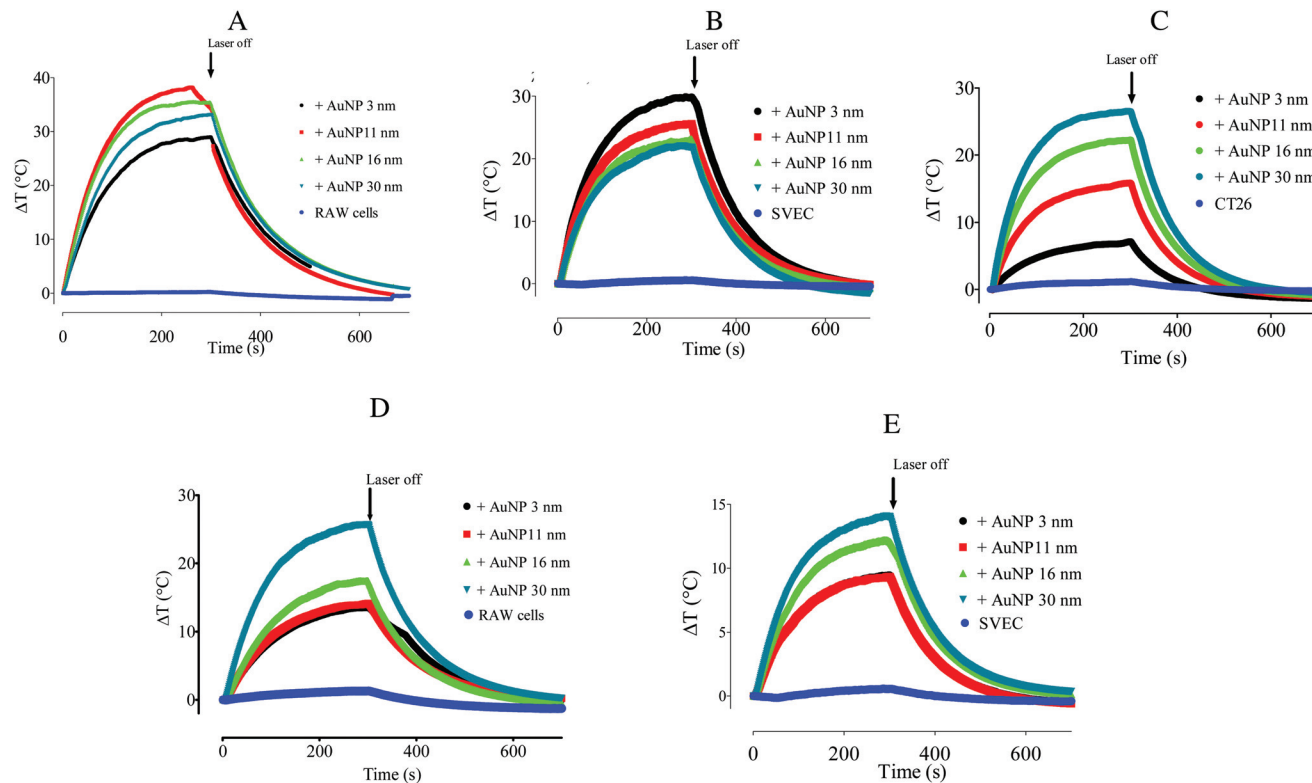


Fig. 4 Temperature curves measured for (A, D) RAW264.7 macrophages, (B, E) SVEC4.10 endothelial cells, and (C) CT26 colon carcinoma cells loaded (or not) with 3, 11, 16, and 30 nm-AuNP ($10 \mu\text{g mL}^{-1}$, 24 h incubation). The cells were irradiated with a 680 nm-laser (A, B, C) or with an 808 nm-laser (D, E) for 5 minutes at 3.57 W cm^{-2} and then the laser was switched off.

16 nm-AuNPs or 16 nm-AuNP-5FU complexes were injected intratumorally at the same Au dose ($40 \mu\text{g}$) when the tumor volume reached $150\text{--}200 \text{ mm}^3$. The tumor was irradiated 24 hours later at 2 W cm^{-2} for 15 min, and the surface temperature of the tumor was monitored (Fig. 5B). Interestingly, whereas the non-injected tumors presented an average temperature of $39.00 \pm 0.70 \text{ }^\circ\text{C}$, the tumors injected with 16 nm AuNPs displayed a higher temperature ($44.60 \pm 1.64 \text{ }^\circ\text{C}$ on average) as compared to those injected with the preformed 16 nm AuNP-5FU ($42.00 \pm 2.40 \text{ }^\circ\text{C}$ on average). Although we cannot be certain whether the 16 nm-AuNP were internalized by cells within the tumor niche, this result is indicative of the impact that the tumor microenvironment has on AuNP plasmonic properties. Since the tumor microenvironment comprises different cell types including tumor cells, macrophages, and endothelial cells, taking into consideration the results on a fractal arrangement inside cells, this suggests that NIR-transparent AuNPs can be converted to NIR-absorbent nanoparticles upon intracellular aggregation-induced plasmon coupling once they are internalized by cells *in vivo*. Another possibility is that the extracellular matrix of the tumor microenvironment, as well as low pH, also triggers the aggregation of nanoparticles. In contrast, the NIR-absorbent 16 nm AuNP-5FU complexes did not show any added value over their isolated building blocks in terms of heating efficiency in the tumor microenvironment. Therefore, we have shown that cell

internalization of AuNP-5FU does not drastically change their heating power; however, it is plausible that the AuNP-5FU complexes have a less homogeneous distribution and a lower cellular uptake than the smallest 16 nm-AuNPs in the tumor microenvironment.^{33,63,64}

Apart from thermal monitoring, another signature of light-to-heat conversion by nanoparticles is the photoacoustic imaging (PAI). We performed PAI in agarose phantoms containing 16 nm-AuNPs or the AuNP-5FU complexes. As expected from the optical properties, the PAI spectrum in the 650–1000 nm range displayed a peak at around 700 nm only for the AuNP-5FU complexes and not for isolated AuNPs, thus confirming plasmon coupling in drug-nanoparticle clusters (Fig. 5C). However, when looking at the PAI signal at the excitation wavelength of 710 nm in tumors, we could see that it was similarly increased after the injection of isolated 16 nm-AuNPs, in comparison with AuNP-5FU complexes, and was visible in some areas of the tumor at 24 hours. This confirmed the light-to-heat conversion of aggregated AuNPs and their complexes in the tumor microenvironment.

Overall, we have shown that the pre-aggregation of spherical AuNPs with a diameter of 16 nm is not necessary for inducing efficient heating in the tumor microenvironment and, contrariwise, the standard coating of spherical AuNPs with citrate could enable cell internalization, intracellular fractal aggregation, and efficient light-to-heat conversion in different cells of



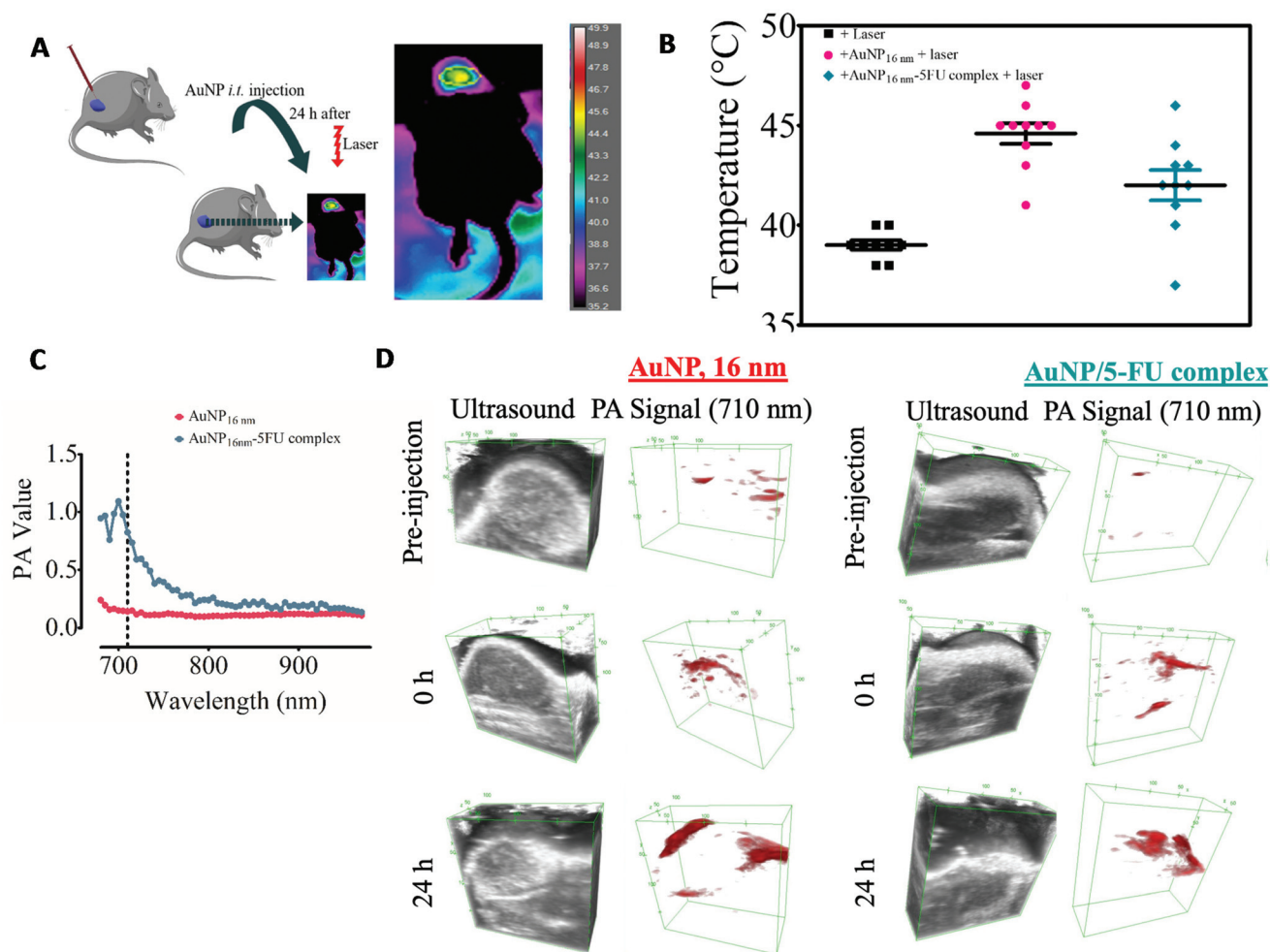


Fig. 5 The *in vivo* photo-thermal activation of CT26 subcutaneous tumors injected intratumorally with 16 nm-AuNPs or the 16 nm AuNP-5FU complex. (A) Scheme of the experimental set-up; tumors were irradiated with an 808 nm laser at 1.94 W cm^{-2} for 15 minutes at 24 hours post-injection of AuNPs and AuNPs-5FU ($40 \mu\text{g}$ per tumor). An example of an *in vivo* infrared thermal image of tumors is shown. (B) The average surface temperature of the tumors during laser irradiation without the injection of nanoparticles (laser only) ($n = 7$) and with intratumoral injection of AuNPs ($n = 10$) and AuNP-5FU ($n = 9$). (C) Photoacoustic (PA) signal spectra of 16 nm-AuNPs and 16 nm AuNP-5FU complexes in agarose gel. (D) Ultrasound B mode imaging and photoacoustic imaging at 710 nm laser excitation of tumors before the injection of nanoparticles, just after intratumoral administration of AuNPs or AuNP-5FU, and 24 hours after.

the tumor microenvironment. In a pioneering study, Hainfeld *et al.* demonstrated that when ~ 18 nm anti-tumor antibody-coated AuNP reached the tumor *in vivo*, nanoparticles were internalized and clustered by the exposure of carboxylic residues upon the enzymatic digestion of antibodies in the acidic endosomal environment.⁶⁵ This approach has shown promising results to ensure a tumor-specific infrared light-absorber conversion of conventional spherical AuNP,⁶⁵ which tackles the undesired overheating of healthy tissue during the photothermal approach. Therefore, it can ensure a better photothermal and optoacoustic performance that complies with both safety and efficacy by tuning the LSPR properties of canonical spherical gold nanoparticles directly *in situ* in the tumor environment. Controllable aggregation of AuNPs in response to the microenvironment properties also proved to be an efficient approach to triggering NIR plasmonic hyperthermia.

For example, the pH⁶ and the presence of electrolytes⁵ can modulate the coalescence of AuNP into clusters. This strategy has yielded some promising results where the simple salt- or pH-induced AuNP aggregation has proved to be an efficient tool for thermal tumor ablation.^{31,65} In our case, however, there is no need for the complicated chemical modification of AuNPs for tumor microenvironment to convert them to NIR light absorbers. Here, citrate-coated AuNPs can agglomerate driven by the protonation of carboxylic groups, thereby leading to nanoparticle coalescence inside an acidic endosomal microenvironment, recapitulating what occurs in aqueous solution.⁶ Recent reports also addressed the utility of macrophages as a delivery vehicle for photothermal therapy in cancer. However, most of these investigations used bona fide NIR-absorbent gold nanoparticles, such as gold nanorods and gold-silica nanoparticles.^{66–69} Here, we proved that NIR transparent



AuNPs are internalized by macrophages, endothelial or cancer cells, and endolysosome-driven plasmon coupling occurred, leading to the thermal conversion of 808 nm light. This is in concordance with a previous report where intracellular spherical gold nanoparticle facilitated the formation of $\cdot\text{O}_2$ singlets for photodynamic therapy.⁷⁰ Importantly, endocytosis-induced plasmon coupling can be efficient enough to generate photoacoustic signals even for small sizes of AuNP (<30 nm)¹³ with the advantages over larger NIR-absorbing gold nanorods or nanostars, to better penetrate the tumor and facilitate the elimination or degradation of gold nanoparticles.³⁵

Correlating intracellular clustering of AuNPs with heating efficiency

Plasmon coupling is highly dependent on the distance between particles, the average number of neighbors, the number of coupled nanoparticles, and the inner organization of the cluster.^{53,55} The plasmon coupling effect and its association with the appearance of a secondary LSPR were well demonstrated by the conformation of discrete dimers and trimers of 60 nm AuNPs that exhibited a secondary LSPR at ~690 nm and ~670 nm, respectively,³⁸ and of linear, globular,

or fractal clusters.^{13,39,40,53} However, few studies have focused on the plasmon coupling phenomenon in cells.^{11,12} Besides, the capacity for light-to-heat conversion is not directly predicted by the optical absorption spectrum and it depends on various parameters such as the size and organization of the nanoparticle clusters and the cellular environments of the clusters. The final temperature in the cell pellet is not only related to the amount of absorbed energy, but also the capacity of the nanoparticle assemblies to convert this absorbed energy into heat and to transfer it to the surrounding medium. In this study, we have combined, for the first time, a comprehensive characterization of the intracellular structures of different sized AuNPs, with the measurements of their optical properties and photothermal efficiency in three different cell types. Thus, a set of descriptors is available and can be analyzed by multivariate analysis to shed light on the potential correlations linking intracellular nanoparticle clustering with heating efficiency, or any of the descriptors. The variables are listed in Table 1. ESI Table S1† displays the average value of these variables for each condition.

Principal component analysis (PCA) was performed to visualize the average behavior in each condition and its depen-

Table 1 Summary of the variables describing the intracellular AuNP cluster and their optical and photothermal properties

Variable	Method of measurement	Description	Unit
NP_diam	TEM	Nanoparticle core size	nm
Lyso_area	TEM	Endolysosome area	nm ²
Clust_diam	TEM	Intracellular cluster diameter	nm
Nb_NPs_clust	TEM	Number of AuNP per intracellular cluster	No unit
Surf_frac	TEM	AuNP surface fraction in endolysosome	%
ELC_dens	TEM	ELC endolysosome density	nm ⁻²
2D_FD	TEM	2D fractal dimension	No unit
Plasm_wl	UV visible spectroscopy	2 nd LSPR wavelength	nm
Plasm_int	UV visible spectroscopy	2 nd LSPR intensity	No unit
DeltaT_680	Photothermal measurements	Temperature increment after 5 min of 680 nm laser irradiation	°C
DeltaT_808	Photothermal measurements	Temperature increment after 5 min of 808 nm laser excitation	°C

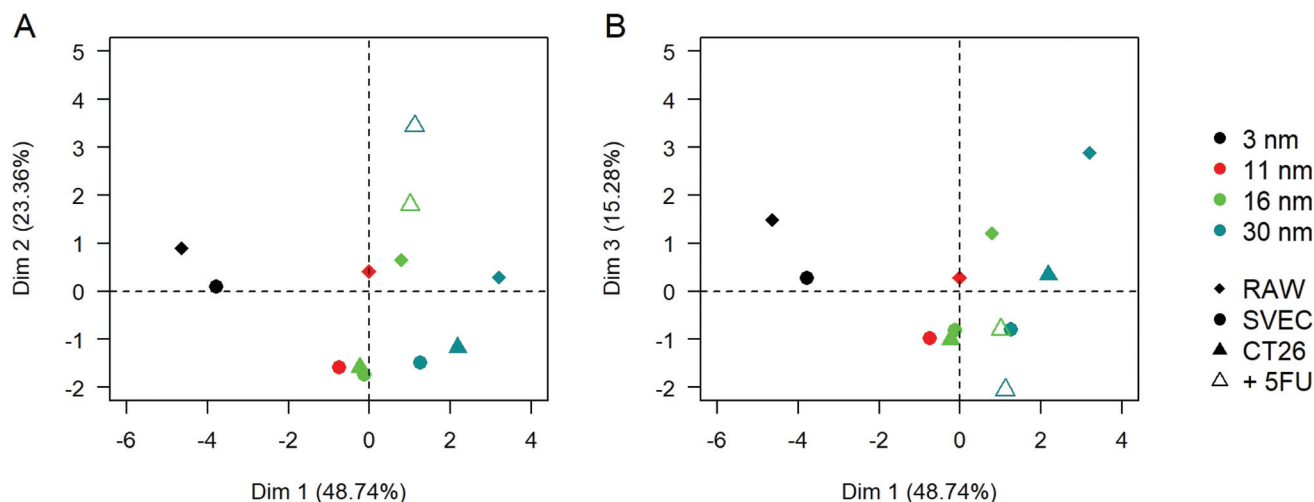


Fig. 6 The principal component analysis was performed on AuNPs-loaded cell properties and cluster characterizations. (A) First and second principal components. (B) First and third principal components.



dence on the different variables. It also allows the quantification of the relative weights of statistically relevant effects (Fig. 6). Using the variables in Table 1, the three first principal components of the PCA, along with which the variation in the data is maximal, respectively represent 51.8%, 24.5%, and 15.7% of the total variance of the results. The projection of the average behavior of the samples onto this 3-dimensional space reveals that the first dimension separates the samples depending on the AuNP core size, the second according to their pre-aggregation state by complexation with 5FU, and the third one tends to separate the RAW macrophages from the two other

cell types. These results are globally consistent with the empirical observations reported above based on the bi-parametric comparison. However, this PCA analysis points out the order of importance of the explored parameters. The correlation between the PCA dimensions and the initial variables can be found in ESI Table S2.† The initial gold nanoparticle size plays a dominant role in the features of intracellular clusters and their optical and photothermal properties. The effect of AuNP size is far beyond the pre-aggregation state of the AuNPs and the cell type. The second dimension of the PCA that distinguishes the pre-aggregated AuNPs from

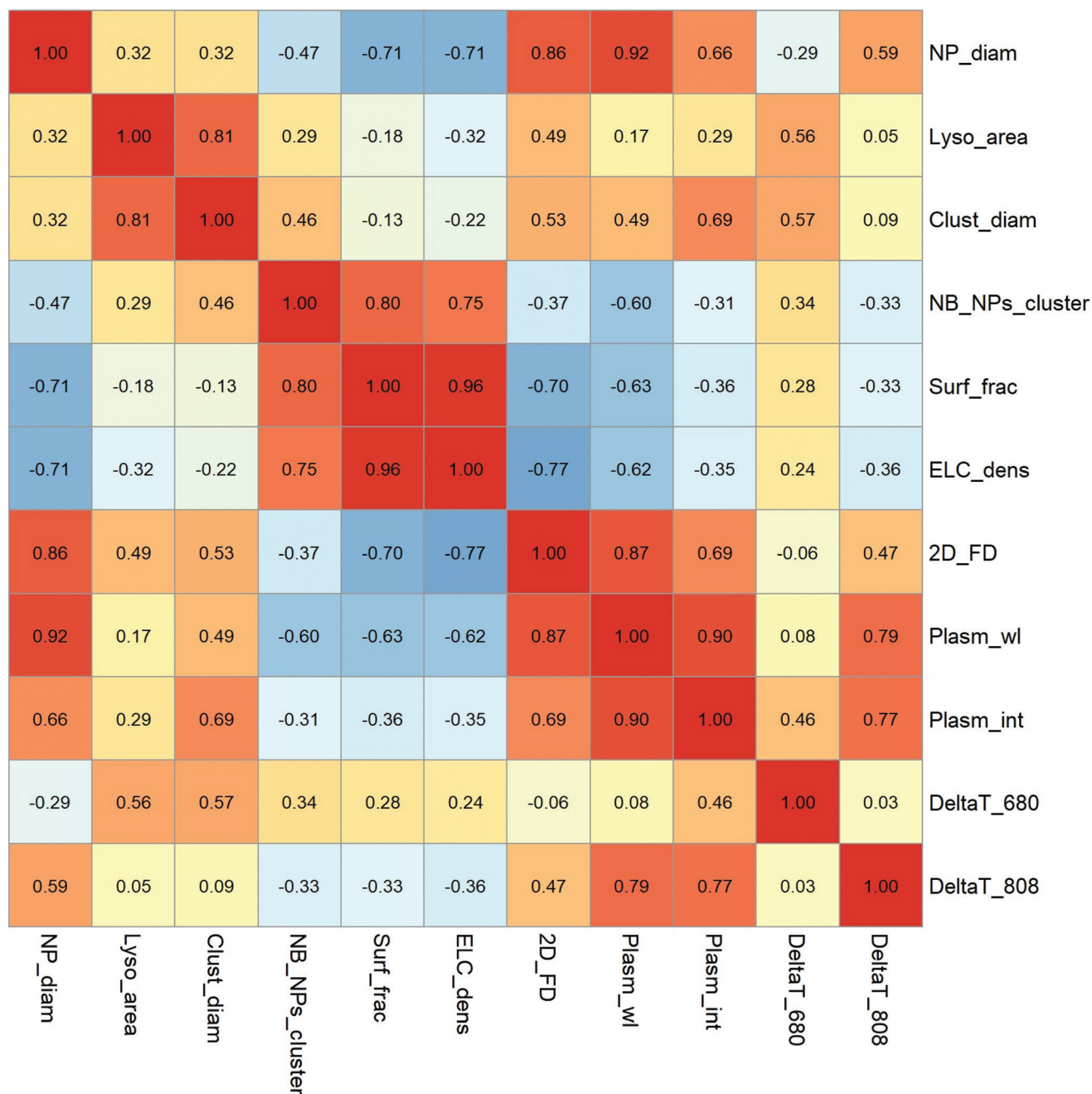


Fig. 7 The heatmap of Pearson's correlation coefficients between each pair of variables.



isolated AuNPs correlates mostly with the aggregate and endolysosome size, as well as the number of AuNPs per cluster; *i.e.*, mostly the cluster properties. In contrast, the third dimension, which differentiates the macrophages from the cancerous and endothelial cells, correlated mostly with the final optical properties of the aggregate and its heating properties at 680 nm.

The correlations between the variables were also studied by the calculation of the Pearson coefficient between each pair of variables (Fig. 7). Looking at the structural parameters describing the intracellular aggregates, we can see some interesting features of endocytosis-driven nanoparticle aggregation. Regarding the cell response to nanoparticle uptake, we observed that the endolysosome area was poorly correlated with the size of the AuNPs ($r_{\text{lyso_area}/\text{NP_diam}} = 0.32$) but tended to shape the AuNPs cluster by adapting the lysosome size to the cluster size ($r_{\text{lyso_area}/\text{Clust_diam}} = 0.81$). The cluster size itself was weakly correlated with the AuNP diameter ($r_{\text{Clust_diam}/\text{NP_diam}} = 0.32$), which is an important aspect of lysosomal confinement in this range of nanoparticle size.

Consistent with the correlation of endolysosome size and cluster size, the number of AuNPs per cluster correlates well with the endolysosome-limited cluster (ELC) density and with the surface fraction covered by AuNPs in endolysosomes. We also confirmed that the 2D fractal dimension of the clusters correlates with the size of AuNP building blocks, showing a higher compacity of large AuNPs clusters ($r_{\text{2D_FD}/\text{NP_diam}} = 0.86$). However, the endolysosome surface fraction covered by AuNPs, as well as the ELC density, correlates negatively with the 2D fractal dimension and AuNP size, showing that globular aggregates of large AuNPs do not fill the endolysosomes as efficiently as loose fractal structures of tiny AuNPs ($r_{\text{Surf_frac}/\text{2D_FD}} = -0.70$, $r_{\text{ELC_dens}/\text{2D_FD}} = -0.77$). This is also consistent with the fact that the number of AuNPs per cluster correlates negatively with the NP size ($r_{\text{NB_NPs_cluster}/\text{NP_diam}} = -0.47$).

Having this general description of the lysosomal clustering of AuNPs in mind, we can examine how it affects the optical properties of AuNPs. The wavelength of the 2nd LSPR is primarily correlated with the size of AuNPs and fractal dimension of the intracellular clusters ($r_{\text{Plasm_wl}/\text{NP_diam}} = 0.92$; $r_{\text{Plasm_wl}/\text{2D_FD}} = 0.87$). This is also true for the intensity of the 2nd LSPR, suggesting that compact aggregates of large particles (even with a small number of NPs) create intense plasmon coupling, which shifts and enhances the 2nd LSPR band. On the other hand, the shift in the 2nd LSPR correlates negatively with the ELC density and endolysosome surface fraction in our conditions, which means that the intracellular confinement of numerous 3 nm or 11 nm AuNPs in a loose structure might not be sufficient to induce plasmon coupling. Interestingly, the appearance and NIR shift of the 2nd LSPR are the key parameters governing the intracellular heating efficiency at 808 nm ($r_{\text{DeltaT}_{808}/r_{\text{Plasma_wl}}} = 0.79$, $r_{\text{DeltaT}_{808}/r_{\text{Plasma_int}}} = 0.77$). At this higher wavelength, the AuNP core size and fractal dimension play the major roles ($r_{\text{DeltaT}_{808}/\text{NP_diam}} = 0.59$, $r_{\text{DeltaT}_{808}/\text{2D_FD}} = 0.47$), while cluster diameter has no influence on heating

efficiency under 808 nm excitation. More surprisingly, the heating efficiency at 680 nm excitation is not correlated with the same variables as the 808 nm excitation. It does not depend on the 2nd LSPR position, as for all NP sizes the plasmon spectra encompass the 680 nm excitation. Moreover, regarding the relationship between the aggregate structure and the 680 nm heating power, it is more sensitive to the cluster diameter, but not to the fractal dimension of the aggregates ($r_{\text{DeltaT}_{680}/\text{Cluster_diam}} = 0.57$; $r_{\text{DeltaT}_{680}/\text{2D_FD}} = -0.06$). Hence, depending on the wavelength of excitation, the details of intracellular clustering might have opposite implications. The massive internalization of ultrasmall AuNPs forming large and loose aggregates in the endolysosomes can be beneficial for excitation close to 680 nm wavelength. It is important to note that this statistical analysis must be handled with caution as they are calculated on only 12 different conditions and the describing variables are not independent of the others. However, it offers a framework for deciphering subtle phenomena linking the intracellular internalization of nanoparticles with their physical properties. Such an analysis, like a quantitative structure–activity relationship, can be extended to a variety of physical phenomena of importance for the therapeutic or diagnostic applications of nanoparticles, taking into account their biological media of application.

Conclusions

Herein, we provide a detailed description of the intracellular clustering of canonical citrate-coated AuNPs in the 3–30 nm size range by three different cell types, namely, macrophages, endothelial cells, and colon cancer cells. We investigated various structural parameters by TEM and SAXS, describing the cell response (endolysosome size) and the nanoparticle clusters formed within the endolysosomes 24 hours after incubation (number of NPs/clusters, cluster size, 2D and 3D fractal dimensions, surface fraction, endolysosome-limited cluster density). A statistical analysis of the data revealed that the cluster size and endolysosome size are correlated but do not depend on the size of the incubated AuNPs in the 3–30 nm range unless preformed aggregates are internalized. The smaller AuNPs occurred in larger numbers, in looser aggregates and covered a greater fraction of the endolysosomes as compared to the largest AuNPs. The 2D and 3D fractal dimensions of intracellular clusters increased with the particle size. This behavior is quite general although we observed some peculiarities of macrophages in comparison to the other cell types. This type of analysis might be useful to model, predict, or correlate the physical properties and the biological outcomes of cell internalized nanoparticles subjected to different excitations. While the same approach could be applied to deciphering intracellular radiosensitization by high-Z nanoparticles, we focused on the plasmonic effects of cell-internalized AuNPs. Collectively, we proved the existence of a plasmon coupling-like process when AuNPs are internalized by cells with a 2nd LSPR band appearing and shifting to the NIR region



when the nanoparticle size and fractal dimension of the intracellular cluster increased. Intracellular plasmon coupling is not directly correlated to the size of the intralysosomal cluster or the number of AuNPs per cluster, but rather the cluster compacity and size of individual AuNPs. The intracellular plasmon-coupling phenomenon translates to an efficient heating efficiency under 808 nm excitation of the three different cell types, with temperature increasing with the AuNP sizes. Intracellular clustering thus transformed NIR-transparent canonical AuNPs with sizes below 30 nm into NIR-absorbing clusters, allowing the simple triggering of intracellular heating by nanoparticle internalization in the three cell types or the colon tumor microenvironment 24 hours after injection. When using the preformed NIR-absorbent 16 nm-AuNP-5FU clusters before cell internalization in place of the isolated NIR-transparent AuNPs, we observed larger endolysosomes with a higher density of nanoparticles. However, this translated into a moderate increase in the 808 nm heating efficiency in cells, and a similar or even worse heating in the tumor environment assessed by a thermal camera and photothermal imaging. Hence harnessing the spontaneous clustering of spherical citrate-coated AuNPs by cells might be a valuable strategy for theranostic purposes such as deploying complex engineering to derive NIR-absorbent AuNPs. Isolated AuNPs with a typical size of 16 nm would also better penetrate the tumor tissue and have a chance to be degraded faster in healthy tissues within intracellular endolysosomes.³⁵ Although this study focused on bare citrate AuNP, when it comes to therapeutics or diagnosis, nanoparticle-functionalization is the key to ensuring tissue selectivity, e.g., tumor antigen-specific antibody⁷¹ and aptamers,²⁹ thus ensuring that the nanoparticles selectively target the tissue of interest. Also, the use of a rather focused laser facilitates the irradiation of the desired tissue area, avoiding damage to healthy tissue. These strategies can augment the internalization of single NIR-invisible AuNP by target cells and can properly benefit from the plasmon coupling effect. Our paper sheds light on the complexity of AuNP distribution and reorganization once internalized by cells, and proposes a general method to link their intracellular fates to their *in situ* physical properties exploited in medical applications.

Conflicts of interest

The authors declare no competing financial interests.

Acknowledgements

This work has received funding from the European Union's Horizon 2020 research and innovation program under grant agreement No 685795 and 801305. The authors thank the ANR CarGold-16-CE09-026, ANR Coligomere-18-CE06-0006 and ANR CycLys-18-CE09-0015-01. VMA received a Post-doc fellowship from Association pour le Recherche contre le Cancer (ARC, Aides Individuelles, post-doctorant, dossier 20150603405).

ANB received a PhD fellowship by the Institute thematique multi-organismes (ITMO) Cancer and the doctoral school Frontières du Vivant (FdV) – Programme Bettencourt. AB received a PhD fellowship by the doctoral school Physique en Ile de France (EDPIF). This work was supported by the ITMO-Inserm Plan Cancer 2014-2019. We are grateful to Christine Péchoux (INRA, UMR 1313, Plateforme MIMA2, Jouy en Josas, France) for electron microscopy preparation and observation. We acknowledge Thomas Bizien (Synchrotron SOLEIL, St-Aubin, France) for his assistance during SAXS experiments. We acknowledge Rémi Le Borgne from the ImagoSeine core facility of the Institut Jacques Monod (UMR7592, CNRS/Université de Paris, Paris, France) for his assistance during TEM observations.

References

- 1 M. A. Dobrovolskaia, A. K. Patri, J. Zheng, J. D. Clogston, N. Ayub, P. Aggarwal, B. W. Neun, J. B. Hall and S. E. McNeil, Interaction of Colloidal Gold Nanoparticles with Human Blood: Effects on Particle Size and Analysis of Plasma Protein Binding Profiles, *Nanomedicine*, 2009, 5(2), 106–117, DOI: 10.1016/j.nano.2008.08.001.
- 2 S. Kittler, C. Greulich, J. S. Gebauer, J. Diendorf, L. Treuel, L. Ruiz, J. M. Gonzalez-Calbet, M. Vallet-Regi, R. Zellner, M. Köller and M. Epple, The Influence of Proteins on the Dispersability and Cell-Biological Activity of Silver Nanoparticles, *J. Mater. Chem.*, 2010, 20(3), 512–518, DOI: 10.1039/b914875b.
- 3 D. P. Lacerda, S. H. Park, J. J. Meuse, C. Pristiniski, D. Becker, M. L. Karim, A. Douglas and J. F. Interaction of Gold Nanoparticles with Common Human Blood Proteins, *ACS Nano*, 2010, 4(1), 365–379, DOI: 10.1021/nn9011187.
- 4 M. P. Monopoli, D. Walczyk, A. Campbell, G. Elia, I. Lynch, F. Baldelli Bombelli and K. A. Dawson, Physical–Chemical Aspects of Protein Corona: Relevance to *in Vitro* and *in Vivo* Biological Impacts of Nanoparticles, *J. Am. Chem. Soc.*, 2011, 133(8), 2525–2534, DOI: 10.1021/ja107583h.
- 5 S. Aryal, R. Bahadur, N. Bhattarai, C. K. Kim and H. Y. Kim, Study of Electrolyte Induced Aggregation of Gold Nanoparticles Capped by Amino Acids, *J. Colloid Interface Sci.*, 2006, 299(1), 191–197, DOI: 10.1016/j.jcis.2006.01.045.
- 6 K. Wagers, T. Chui and S. Adem, Effect of PH on the Stability of Gold Nanoparticles and Their Application for Melamine Detection in Infant Formula, *IOSR J. Appl. Chem. Ver II*, 2014, 7(8), 15–20.
- 7 L. Tian, A. Chang and M. P. Melancon, Exploring Gold Nanoparticle Interactions with Proteins and the Tumor Microenvironment in Biological Systems, *Transl. Cancer Res.*, 2017, 6(Suppl 2), S309–S312, DOI: 10.21037/tcr.2017.03.53.
- 8 M. L. Etheridge, K. R. Hurley, J. Zhang, S. Jeon, H. L. Ring, C. Hogan, C. L. Haynes, M. Garwood and J. C. Bischof, Accounting for Biological Aggregation in Heating and



- Imaging of Magnetic Nanoparticles, *Technology*, 2014, **2**(3), 214–228, DOI: 10.1142/S2339547814500198.
- 9 J. G. Ovejero, D. Cabrera, J. Carrey, T. Valdivielso, G. Salas and F. J. Teran, Effects of Inter- and Intra-Aggregate Magnetic Dipolar Interactions on the Magnetic Heating Efficiency of Iron Oxide Nanoparticles, *Phys. Chem. Chem. Phys.*, 2016, **18**(16), 10954–10963, DOI: 10.1039/C6CP00468G.
 - 10 D. F. Coral, P. Mendoza Zélis, M. Marciello, M. d. P. Morales, A. Craievich, F. H. Sánchez and M. B. Fernández van Raap, Effect of Nanoclustering and Dipolar Interactions in Heat Generation for Magnetic Hyperthermia, *Langmuir*, 2016, **32**(5), 1201–1213, DOI: 10.1021/acs.langmuir.5b03559.
 - 11 A. L. Chen, Y. S. Hu, M. A. Jackson, A. Y. Lin, J. K. Young, R. J. Langsner and R. A. Drezek, Quantifying Spectral Changes Experienced by Plasmonic Nanoparticles in a Cellular Environment to Inform Biomedical Nanoparticle Design, *Nanoscale Res. Lett.*, 2014, **9**(1), 454, DOI: 10.1186/1556-276X-9-454.
 - 12 A. C. Curry, M. Crow and A. Wax, Molecular Imaging of Epidermal Growth Factor Receptor in Live Cells with Refractive Index Sensitivity Using Dark-Field Microspectroscopy and Immunotargeted Nanoparticles, *J. Biomed. Opt.*, 2008, **13**(1), 014022, DOI: 10.1117/1.2837450.
 - 13 S. Han, R. Bouchard and K. V. Sokolov, Molecular Photoacoustic Imaging with Ultra-Small Gold Nanoparticles, *Biomed. Opt. Express*, 2019, **10**(7), 3472–3483, DOI: 10.1364/BOE.10.003472.
 - 14 A. Espinosa, J. Kolosnjaj-Tabi, A. Abou-Hassan, A. Plan Sangnier, A. Curcio, A. K. A. Silva, R. Di Corato, S. Neveu, T. Pellegrino, L. M. Liz-Marzán and C. Wilhelm, Magnetic (Hyper)Thermia or Photothermia? Progressive Comparison of Iron Oxide and Gold Nanoparticles Heating in Water, in Cells, and In Vivo, *Adv. Funct. Mater.*, 2018, **28**(37), 1803660, DOI: 10.1002/adfm.201803660.
 - 15 P. Retif, S. Pinel, M. Toussaint, C. Frochot, R. Chouikrat, T. Bastogne and M. Barberi-Heyob, Nanoparticles for Radiation Therapy Enhancement: The Key Parameters, *Theranostics*, 2015, **5**(9), 1030–1044, DOI: 10.7150/thno.11642.
 - 16 S. Gudlur, C. Sandén, P. Matoušková, C. Fasciani and D. Aili, Liposomes as Nanoreactors for the Photochemical Synthesis of Gold Nanoparticles, *J. Colloid Interface Sci.*, 2015, **456**, 206–209, DOI: 10.1016/j.jcis.2015.06.033.
 - 17 A. K. Rengan, M. Jagtap, A. De, R. Banerjee and R. Srivastava, Multifunctional Gold Coated Thermo-Sensitive Liposomes for Multimodal Imaging and Photo-Thermal Therapy of Breast Cancer Cells, *Nanoscale*, 2014, **6**(2), 916–923, DOI: 10.1039/c3nr04448c.
 - 18 J. Xie, Q. Zhang, J. Y. Lee and D. I. C. Wang, The Synthesis of SERS-Active Gold Nanoflower Tags for in Vivo Applications, *ACS Nano*, 2008, **2**(12), 2473–2480, DOI: 10.1021/nn800442q.
 - 19 R. Cheheltani, R. M. Ezzibdeh, P. Chhour, K. Pulaparthi, J. Kim, M. Jurcova, J. C. Hsu, C. Blundell, H. I. Litt, V. A. Ferrari, H. R. Allcock, C. M. Sehgal and D. P. Cormode, Tunable, Biodegradable Gold Nanoparticles as Contrast Agents for Computed Tomography and Photoacoustic Imaging, *Biomaterials*, 2016, **102**, 87–97, DOI: 10.1016/j.biomaterials.2016.06.015.
 - 20 F. Kretschmer, U. Mansfeld, S. Hoepfner, M. D. Hager and U. S. Schubert, Tunable Synthesis of Poly(Ethylene Imine)–Gold Nanoparticle Clusters, *Chem. Commun.*, 2014, **50**(1), 88–90, DOI: 10.1039/C3CC45090B.
 - 21 W. Li and X. Chen, Gold Nanoparticles for Photoacoustic Imaging, *Nanomedicine*, 2015, **10**(2), 299–320, DOI: 10.2217/nnm.14.169.
 - 22 M. H. Oh, J. H. Yu, I. Kim and Y. S. Nam, Genetically Programmed Clusters of Gold Nanoparticles for Cancer Cell-Targeted Photothermal Therapy, *ACS Appl. Mater. Interfaces*, 2015, **7**(40), 22578–22586, DOI: 10.1021/acsami.5b07029.
 - 23 Y. Liu, J. He, K. Yang, C. Yi, Y. Liu, L. Nie, N. M. Khashab, X. Chen and Z. Nie, Folding Up of Gold Nanoparticle Strings into Plasmonic Vesicles for Enhanced Photoacoustic Imaging, *Angew. Chem., Int. Ed.*, 2015, **54**(52), 15809–15812, DOI: 10.1002/anie.201508616.
 - 24 M. Hu, J. Chen, Z.-Y. Li, L. Au, G. V. Hartland, X. Li, M. Marquez and Y. Xia, Gold Nanostructures: Engineering Their Plasmonic Properties for Biomedical Applications, *Chem. Soc. Rev.*, 2006, **35**(11), 1084–1094, DOI: 10.1039/b517615h.
 - 25 A. Sambou, B. D. Ngom, L. Gomis and A. C. Beye, Turnability of the Plasmonic Response of the Gold Nanoparticles in Infrared Region, *Am. J. Nanomater.*, 2016, **4**(3), 63–69, DOI: 10.12691/ajn-4-3-3.
 - 26 S. K. Ghosh and T. Pal, Interparticle Coupling Effect on the Surface Plasmon Resonance of Gold Nanoparticles: From Theory to Applications, *Chem. Rev.*, 2007, **107**(11), 4797–4862, DOI: 10.1021/cr0680282.
 - 27 H. Lange, B. H. Juárez, A. Carl, M. Richter, N. G. Bastús, H. Weller, C. Thomsen, R. von Klitzing and A. Knorr, Tunable Plasmon Coupling in Distance-Controlled Gold Nanoparticles, *Langmuir*, 2012, **28**(24), 8862–8866, DOI: 10.1021/la3001575.
 - 28 P. K. Jain and M. A. El-Sayed, Plasmonic Coupling in Noble Metal Nanostructures, *Chem. Phys. Lett.*, 2010, **487**(4–6), 153–164, DOI: 10.1016/j.cplett.2010.01.062.
 - 29 Y. Bai, F. Feng, L. Zhao, C. Wang, H. Wang, M. Tian, J. Qin, Y. Duan and X. He, Aptamer/Thrombin/Aptamer-AuNPs Sandwich Enhanced Surface Plasmon Resonance Sensor for the Detection of Subnanomolar Thrombin, *Biosens. Bioelectron.*, 2013, **47C**, 265–270, DOI: 10.1016/j.bios.2013.02.004.
 - 30 M. Sriram, K. Zong, S. R. C. Vivekchand and J. J. Gooding, Single Nanoparticle Plasmonic Sensors, *Sensors*, 2015, 25774–25792, DOI: 10.3390/s151025774.
 - 31 M. Sun, F. Liu, Y. Zhu, W. Wang, J. Hu, J. Liu, Z. Dai, K. Wang, Y. Wei, J. Bai and W. Gao, Salt-Induced



- Aggregation of Gold Nanoparticles for Photoacoustic Imaging and Photothermal Therapy of Cancer, *Nanoscale*, 2016, **8**(8), 4452–4457, DOI: 10.1039/C6NR00056H.
- 32 J. Song, G. Niu and X. Chen, Amphiphilic-Polymer-Guided Plasmonic Assemblies and Their Biomedical Applications, *Bioconjugate Chem.*, 2017, **28**(1), 105–114, DOI: 10.1021/acs.bioconjchem.6b00521.
- 33 S. D. Perrault, C. Walkey, T. Jennings, H. C. Fischer and W. C. W. Chan, Mediating Tumor Targeting Efficiency of Nanoparticles through Design, *Nano Lett.*, 2009, **9**(5), 1909–1915, DOI: 10.1021/nl900031y.
- 34 E. A. Sykes, J. Chen, G. Zheng and W. C. W. Chan, Investigating the Impact of Nanoparticle Size on Active and Passive Tumor Targeting Efficiency, *ACS Nano*, 2014, **8**(6), 5696–5706, DOI: 10.1021/nn500299p.
- 35 A. Balfourier, N. Luciani, G. Wang, G. Lelong, O. Ersen, A. Khelifa, D. Alloyeau, F. Gazeau and F. Carn, Unexpected Intracellular Biodegradation and Recrystallization of Gold Nanoparticles, *Proc. Natl. Acad. Sci. U. S. A.*, 2020, **117**(1), 103, DOI: 10.1073/pnas.1911734116.
- 36 M. Liu, Q. Li, L. Liang, J. Li, K. Wang, J. Li, M. Lv, N. Chen, H. Song, J. Lee, J. Shi, L. Wang, R. Lal and C. Fan, Real-Time Visualization of Clustering and Intracellular Transport of Gold Nanoparticles by Correlative Imaging, *Nat. Commun.*, 2017, **8**(May), 1–10, DOI: 10.1038/ncomms15646.
- 37 P. Nativo, I. A. Prior and M. Brust, Uptake and Intracellular Fate of Surface-Modified Gold Nanoparticles, *ACS Nano*, 2008, **2**(8), 1639–1644, DOI: 10.1021/nn800330a.
- 38 C. Schopf, E. Noonan, A. Quinn and D. Iacopino, Self-Assembly of Gold Nanocrystals into Discrete Coupled Plasmonic Structures, *Crystals*, 2016, **6**(9), 117, DOI: 10.3390/cryst6090117.
- 39 Y. A. Wang, X. Yu, P. M. Silverman, R. L. Harris and H. E. Egelman, The structure of F-pili, *J. Mol. Biol.*, 2010, **385**(1), 22–29, DOI: 10.1016/j.jmb.2008.10.054.
- 40 S. P. Scheeler, S. Mühlig, C. Rockstuhl, S. B. Hasan, S. Ullrich, F. Neubrech, S. Kudera and C. Pacholski, Plasmon Coupling in Self-Assembled Gold Nanoparticle-Based Honeycomb Islands, *J. Phys. Chem. C*, 2013, **117**(36), 18634–18641, DOI: 10.1021/jp405560t.
- 41 N. G. Bastús, J. Comenge and V. Puntès, Kinetically Controlled Seeded Growth Synthesis of Citrate-Stabilized Gold Nanoparticles of up to 200 Nm: Size Focusing versus Ostwald Ripening, *Langmuir*, 2011, **27**(17), 11098–11105, DOI: 10.1021/la201938u.
- 42 J. Piella, N. G. Bastús and V. Puntès, Size-Controlled Synthesis of Sub-10-Nanometer Citrate-Stabilized Gold Nanoparticles and Related Optical Properties, *Chem. Mater.*, 2016, **28**(4), 1066–1075, DOI: 10.1021/acs.chemmater.5b04406.
- 43 J. Teixeira, Small-Angle Scattering by Fractal Systems, *J. Appl. Crystallogr.*, 1988, **21**(6), 781–785, DOI: 10.1107/S0021889888000263.
- 44 N. A-Gonzalez, J. A. Quintana, S. García-Silva, M. Mazariegos, A. González de la Aleja, J. A. Nicolás-Ávila, W. Walter, J. M. Adrover, G. Crainiciuc, V. K. Kuchroo, C. V. Rothlin, H. Peinado, A. Castrillo, M. Ricote and A. Hidalgo, Phagocytosis Imprints Heterogeneity in Tissue-Resident Macrophages, *J. Exp. Med.*, 2017, **214**(5), 1281–1296, DOI: 10.1084/jem.20161375.
- 45 S. Gordon and A. Plüddemann, Tissue Macrophages: Heterogeneity and Functions, *BMC Biol.*, 2017, **15**(1), 53, DOI: 10.1186/s12915-017-0392-4.
- 46 V. Mulens-Arias, A. Balfourier, A. Nicolás-Boluda, F. Carn and F. Gazeau, Disturbance of Adhesomes by Gold Nanoparticles Reveals a Size- and Cell Type-Bias, *Biomater. Sci.*, 2019, **7**(1), 389–408, DOI: 10.1039/C8BM01267A.
- 47 M. Bouda, J. S. Caplan and J. E. Saiers, Box-Counting Dimension Revisited: Presenting an Efficient Method of Minimizing Quantization Error and an Assessment of the Self-Similarity of Structural Root Systems, *Front. Plant Sci.*, 2016, **7**, 149–149, DOI: 10.3389/fpls.2016.00149.
- 48 X. Gu and D. F. R. Mildner, Determination of Porosity in Anisotropic Fractal Systems by Neutron Scattering, *J. Appl. Crystallogr.*, 2018, **51**(1), 175–184, DOI: 10.1107/S1600576718000080.
- 49 D. F. R. Mildner and P. L. Hall, Small-Angle Scattering from Porous Solids with Fractal Geometry, *J. Phys. D: Appl. Phys.*, 1986, **19**(8), 1535–1545, DOI: 10.1088/0022-3727/19/8/021.
- 50 S. Kumari, M. G. S and S. Mayor, Endocytosis Unplugged: Multiple Ways to Enter the Cell, *Cell Res.*, 2010, **20**(3), 256–275, DOI: 10.1038/cr.2010.19.
- 51 W. Sun, L. Luo, Y. Feng, Y. Cai, Y. Zhuang, R.-J. Xie, X. Chen and H. Chen, Aggregation-Induced Emission Gold Clustoluminogens for Enhanced Low-Dose X-Ray-Induced Photodynamic Therapy, *Angew. Chem., Int. Ed.*, 2019, **59**, 9914–9921, DOI: 10.1002/anie.201908712.
- 52 Y. Zhang, F. Huang, C. Ren, J. Liu, L. Yang, S. Chen, J. Chang, C. Yang, W. Wang, C. Zhang, Q. Liu, X.-J. Liang and J. Liu, Enhanced Radiosensitization by Gold Nanoparticles with Acid-Triggered Aggregation in Cancer Radiotherapy, *Adv. Sci.*, 2019, **6**(8), 1801806, DOI: 10.1002/adv.201801806.
- 53 A. Balfourier, V. Mulens-Arias, F. Gazeau and F. Carn, Rational Design of Fractal Gold Nanosphere Assemblies with Optimized Photothermal Conversion Using a Quantitative Structure Property Relationship (QSPR) Approach, *J. Phys. Chem. C*, 2020, **124**, 8938–8948, DOI: 10.1021/acs.jpcc.0c00384.
- 54 V. Mulens-Arias, A. Nicolás-Boluda, A. Gehanno, A. Balfourier, F. Carn and F. Gazeau, Polyethyleneimine-Assisted One-Pot Synthesis of Quasi-Fractal Plasmonic Gold Nanocomposites as a Photothermal Theranostic Agent, *Nanoscale*, 2019, **11**(7), 3344–3359, DOI: 10.1039/C8NR09849B.
- 55 B. Khlebtsov, V. Zharov, A. Melnikov, V. Tuchin and N. Khlebtsov, Optical Amplification of Photothermal Therapy with Gold Nanoparticles and Nanoclusters, *Nanotechnology*, 2006, **17**(20), 5167–5179, DOI: 10.1088/0957-4484/17/20/022.



- 56 S. Soni and R. K. Sinha, Controlling Parameters for Plasmonic Photothermal Ablation of a Tumor, *IEEE J. Sel. Top. Quantum Electron.*, 2016, **22**(4), 21–28, DOI: 10.1109/JSTQE.2016.2514359.
- 57 A. Espinosa, A. K. A. Silva, A. Sánchez-Iglesias, M. Grzelczak, C. Péchoux, K. Desboeufs, L. M. Liz-Marzán and C. Wilhelm, Cancer Cell Internalization of Gold Nanostars Impacts Their Photothermal Efficiency In Vitro and In Vivo: Toward a Plasmonic Thermal Fingerprint in Tumoral Environment, *Adv. Healthcare Mater.*, 2016, **5**(9), 1040–1048, DOI: 10.1002/adhm.201501035.
- 58 A. R. Rastinehad, H. Anastos, E. Wajswol, J. S. Winoker, J. P. Sfakianos, S. K. Doppalapudi, M. R. Carrick, C. J. Knauer, B. Taouli, S. C. Lewis, A. K. Tewari, J. A. Schwartz, S. E. Canfield, A. K. George, J. L. West and N. J. Halas, Gold Nanoshell-Localized Photothermal Ablation of Prostate Tumors in a Clinical Pilot Device Study, *Proc. Natl. Acad. Sci. U. S. A.*, 2019, **116**(37), 18590, DOI: 10.1073/pnas.1906929116.
- 59 A. Plan Sangnier, A. Van de Walle, R. Aufaure, M. Fradet, L. Motte, E. Guénin, Y. Lalatonne and C. Wilhelm, Endosomal Confinement of Gold Nanospheres, Nanorods, and Nanoraspberries Governs Their Photothermal Identity and Is Beneficial for Cancer Cell Therapy, *Adv. Biosyst.*, 2020, **4**(4), 1900284, DOI: 10.1002/adbi.201900284.
- 60 E. D. SoRelle, O. Liba, J. L. Campbell, R. Dalal, C. L. Zavaleta and A. de la Zerda, A Hyperspectral Method to Assay the Microphysiological Fates of Nanomaterials in Histological Samples, *eLife*, 2016, **5**, e16352, DOI: 10.7554/eLife.16352.
- 61 J. Nam, N. Won, H. Jin, H. Chung and S. Kim, PH-Induced Aggregation of Gold Nanoparticles for Photothermal Cancer Therapy, *J. Am. Chem. Soc.*, 2009, **131**(38), 13639–13645, DOI: 10.1021/ja902062j.
- 62 S. Son, N. Kim, D. G. You, H. Y. Yoon, J. Y. Yhee, K. Kim and I. Chan, Theranostics Antitumor Therapeutic Application of Self-Assembled RNAi-AuNP Nanoconstructs: Combination of VEGF-RNAi and Photothermal Ablation, *J. Am. Chem. Soc.*, 2017, **7**(1), 9–22, DOI: 10.7150/thno.16042.
- 63 K. Huang, H. Ma, J. Liu, S. Huo, A. Kumar, T. Wei, X. Zhang, S. Jin, Y. Gan, P. C. Wang, S. He, X. Zhang and X.-J. Liang, Size-Dependent Localization and Penetration of Ultrasmall Gold Nanoparticles in Cancer Cells, Multicellular Spheroids, and Tumors in Vivo, *ACS Nano*, 2012, **6**(5), 4483–4493, DOI: 10.1021/nn301282m.
- 64 S. Huo, H. Ma, K. Huang, J. Liu, T. Wei, S. Jin, J. Zhang, S. He and X.-J. Liang, Superior Penetration and Retention Behavior of 50 Nm Gold Nanoparticles in Tumors, *Cancer Res.*, 2013, **73**(1), 319, DOI: 10.1158/0008-5472.CAN-12-2071.
- 65 J. F. Hainfeld, M. J. O'Connor, P. Lin, L. Qian, D. N. Slatkin and H. M. Smilowitz, Infrared-Transparent Gold Nanoparticles Converted by Tumors to Infrared Absorbers Cure Tumors in Mice by Photothermal Therapy, *PLoS One*, 2014, **9**(2), e88414, DOI: 10.1371/journal.pone.0088414.
- 66 C. Christie, S. J. Madsen, Q. Peng and H. Hirschberg, Photothermal Therapy Employing Gold Nanoparticle-Loaded Macrophages as Delivery Vehicles: Comparing the Efficiency of Nanoshells Versus Nanorods, *J. Environ. Pathol. Toxicol. Oncol.*, 2017, **36**(3), 229–235, DOI: 10.1615/JEnvironPatholToxicolOncol.2017021545.
- 67 Z. Li, H. Huang, S. Tang, Y. Li, X. F. Yu, H. Wang, P. Li, Z. Sun, H. Zhang, C. Liu and P. K. Chu, Small Gold Nanorods Laden Macrophages for Enhanced Tumor Coverage in Photothermal Therapy, *Biomaterials*, 2016, **74**, 144–154, DOI: 10.1016/j.biomaterials.2015.09.038.
- 68 T. D. Yang, W. Choi, T. H. Yoon, K. J. Lee, J.-S. Lee, J. H. Joo, M.-G. Lee, H. S. Yim, K. M. Choi, B. Kim, J. J. Lee, H. Kim, D. Y. Lee, K.-Y. Jung and S.-K. Baek, In Vivo Photothermal Treatment by the Peritumoral Injection of Macrophages Loaded with Gold Nanoshells, *Biomed. Opt. Express*, 2016, **7**(1), 185, DOI: 10.1364/BOE.7.000185.
- 69 C. Christie, S. J. Madsen, Q. Peng and H. Hirschberg, Macrophages as Nanoparticle Delivery Vectors for Photothermal Therapy of Brain Tumors, *Ther. Delivery*, 2015, **6**(3), 371–384, DOI: 10.4155/tde.14.121.
- 70 Y. Yang, Y. Hu, H. Du and H. Wang, Intracellular Gold Nanoparticle Aggregation and Their Potential Applications in Photodynamic Therapy, *Chem. Commun.*, 2014, **50**(55), 7287–7290, DOI: 10.1039/c4cc02376e.
- 71 L. A. Dykman, S. A. Staroverov, A. S. Fomin, V. A. Khanadeev, B. N. Khlebtsov and V. A. Bogatyrev, Gold Nanoparticles as an Adjuvant: Influence of Size, Shape, and Technique of Combination with CpG on Antibody Production, *Int. Immunopharmacol.*, 2018, **54**(June 2017), 163–168, DOI: 10.1016/j.intimp.2017.11.008.

